PROCEEDINGS A

royalsocietypublishing.org/journal/rspa

Review

Cite this article: Dey S, Ali SZ, Padhi E. 2019 Terminal fall velocity: the legacy of Stokes from the perspective of fluvial hydraulics. *Proc. R. Soc. A* **475**: 20190277.
http://dx.doi.org/10.1098/rspa.2019.0277

Received: 7 May 2019
Accepted: 2 August 2019

Subject Areas:
fluid mechanics, geophysics

Keywords:
terminal fall velocity, Stokes law, hydrodynamics, sediment transport

Authors for correspondence:
Subhasish Dey
e-mail: sdey@iitkgp.ac.in
Sk Zeeshan Ali
e-mail: skzeeshanali@iitkgp.ac.in
Ellora Padhi
e-mail: ellora@iitkgp.ac.in

THE ROYAL SOCIETY
PUBLISHING

Terminal fall velocity: the legacy of Stokes from the perspective of fluvial hydraulics

Subhasish Dey[1,2,3], Sk Zeeshan Ali[1] and Ellora Padhi[1]

[1]Department of Civil Engineering, Indian Institute of Technology Kharagpur, Kharagpur, West Bengal 721302, India
[2]Physics and Applied Mathematics Unit, Indian Statistical Institute, Kolkata, West Bengal 700108, India
[3]Department of Hydraulic Engineering, State Key Laboratory of Hydro-Science and Engineering, Tsinghua University, Beijing 100084, People's Republic of China

SD, 0000-0001-9764-1346; SZA, 0000-0003-0763-7437; EP, 0000-0002-2295-2171

This review article, dedicated to the bicentenary celebration of Sir George Gabriel Stokes' birthday, presents the state-of-the-science of terminal fall velocity, highlighting his rich legacy from the perspective of fluvial hydraulics. It summarizes the fluid drag on a particle and the current status of the drag coefficient from both the theoretical and empirical formulations, highlighting the three major realms—Stokesian, transitional and Newtonian realms. The force system that drives the particle motion falling through a fluid is described. The response of terminal fall velocity to key factors, which include particle shape, hindered settling and turbulence (nonlinear drag, vortex trapping, fast tracking and effects of loitering), is delineated. The article puts into focus the impact of terminal fall velocity on fluvial hydraulics, discussing the salient role that the terminal fall velocity plays in governing the hydrodynamics of the sediment threshold, bedload transport and suspended load transport. Finally, an innovative perspective is presented on the subject's future research track, emphasizing open questions.

1. Introduction

When a particle falls through a fluid, it accelerates owing to gravity. The fluid drags the particle in unison

royalsocietypublishing.org/journal/rspa Proc. R. Soc. A 475: 20190277

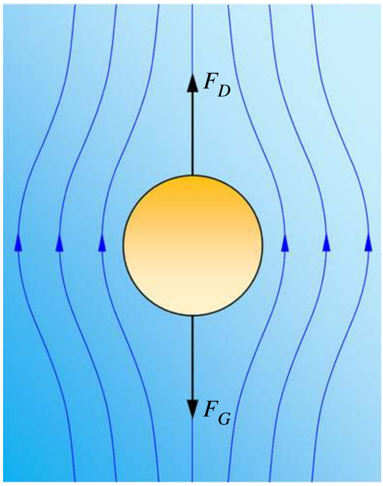

Figure 1. Schematic of terminal fall velocity of a particle. F_D is the fluid drag and F_G is the submerged weight of the particle. Flow streamlines past the particle are also shown. (Online version in colour.)

to reduce its inertia (figure 1). By and by, the acceleration of the particle ceases, and it falls with a constant velocity, called the *terminal fall velocity*. Quantification of the terminal fall velocity is made by balancing the fluid drag F_D and the submerged weight F_G of the particle (figure 1). A precise measure of the terminal fall velocity requires a good understanding of the fluid drag, the importance of which was envisioned long ago by Sir Isaac Newton. However, with regard to the estimation of fluid drag, the name that first comes to mind is Sir George Gabriel Stokes (figure 2), whose astounding contributions to fluid dynamics need no introduction. It is in no way an exaggeration to highlight one of his remarkable papers in the mid-nineteenth century: 'On the effect of the internal friction of fluids on the motion of pendulums', which was published in 1851 in the *Transactions of the Cambridge Philosophical Society*. In this paper, Stokes made the first breakthrough in calculating the fluid drag—also called *Stokes' law*, which defines the *Stokes drag* F_D on a spherical particle of diameter d as

$$F_D = 3\pi \mu U d, \tag{1.1}$$

where μ is the dynamic viscosity of the fluid and U is the free stream velocity. Equation (1.1) is legitimate when the particle Reynolds number $\mathscr{R}(= Ud/\nu)$ remains smaller than unity [1], where ν is the kinematic viscosity of fluid $(= \mu/\rho_f)$ and ρ_f is the mass density of fluid. The applications of Stokes' law are far-reaching. Stokes' law is deemed to have played a subtle role in research leading to the bestowing of at least three Nobel prizes [2]. This law was applied by Millikan in his oil-drop experiment to determine the charge of an electron. In addition, Stokes' law is a key prerequisite to understanding a wide variety of physical processes; for instance, swimming of microorganisms [2], residence time of volcanic stuffs [3,4], and sedimentation of tiny particles in air [5] and water [6]. From the perspective of fluvial hydraulics, terminal fall velocity is among the central parameters to drive some of the key processes of sediment transport. It offers limiting values of *movability number* $M_*(= u_*/w_t)$, which could be used as a guideline to distinguish various modes of sediment transport. Here, u_* is the shear velocity $[= (\tau_b/\rho_f)^{1/2}]$, τ_b is the bed shear stress and w_t is the terminal fall velocity. To be specific, for $M_* \in [1/6, 1/2]$, particles are transported in rolling and sliding modes, called *contact load transport*. For $M_* \in [1/2, 5/3]$, particles are transported in a series of tiny leaps, called *saltation*. In addition, for $M_* > 5/3$, particles are transported as a *suspended load* [6].

After Stokes [1], researchers made impressive strides in their quest to obtain an improved formulation of fluid drag over a rich spectrum of particle Reynolds number $\mathscr{R}$. Despite

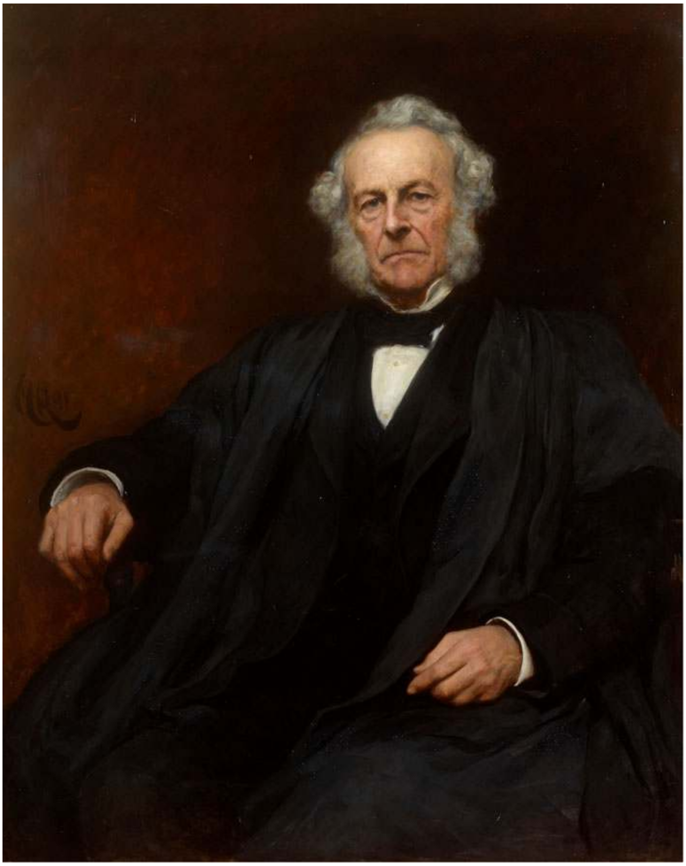

Figure 2. Portrait of George Gabriel Stokes (courtesy of Alice Power, The Royal Society, London). (Online version in colour.)

momentous advances made by the legacies of Stokes, Stokes' law has remained a rule of thumb, for more than 16 decades, in estimating the terminal fall velocity for $\mathscr{R} < 1$. This review article pays tribute to the bicentennial anniversary of George Gabriel Stokes (1819–1903), whose brief biography is furnished below.

George Gabriel Stokes, son of Gabriel Stokes, who was a clergyman, was born on 13 August 1819 in Skreen, County Sligo, Ireland (figure 2). He was brought up at home, where he learnt reading and arithmetic. In 1832, he was admitted to Dr Wall's school, Dublin, and during 1835–1837 he was taught at Bristol College. In 1837, he went to Pembroke College, Cambridge, where his inherent talents attracted attention. He graduated as Senior Wrangler and the first Smith's Prizeman from Pembroke College in 1841, and was elected to a fellowship there. In 1849, he became the Lucasian Professor of Mathematics at the University of Cambridge, a position he held until death. The jubilee of this appointment was celebrated in 1899 in a ceremony where he was presented with a memorial gold medal. In 1857, he married Mary Susanna Robinson. They had five children. As a mathematician, Stokes pioneered Stokes' theorem in vector calculus and made seminal contributions to the theory of asymptotic expansions. Being a physicist, he significantly contributed to fluid dynamics, including the Navier–Stokes equations, and especially to physical optics, with outstanding works on fluorescence and polarization. He made an impressive contribution to the conduction of heat in crystals and to many engineering aspects. He also worked on religion. As a Gifford lecturer, in 1891, he published his works on natural theology. He was also the vice-president of the British and Foreign Bible Society. Stokes received several scientific honours. He was a Knight of the Prussian Order *Pour le Mérite* and a Foreign Associate of the French Institute. He was awarded the Rumford Medal in 1852, Gauss Medal in

1877, Copley Medal in 1893, the Arago Medal in 1899 and the Helmholtz Medal in 1901. He was secretary of the Royal Society during 1854–1885 and president during 1885–1890. In 1889, he was made a baronet. He represented the University of Cambridge in Parliament during 1887–1891. He was selected Master of Pembroke in 1902. About a month before his demise, he managed to attend the annual dinner of the Cambridge Philosophical Society and gave a splendid speech about his cordial connection with the College and the Society. He died on 1 February 1903. On his extraordinary scientific brilliance, one of his colleagues, Sir R. C. Jebb, wrote the following lines on the occasion of the 50th anniversary of his Lucasian Professorship [7]:

> Clear mind, strong heart, true servant of the light,
> True to that light within the soul, whose ray
> Pure and serene, hath brightened on thy way,
> Honour and praise now crown thee on the height
> Of tranquil years. Forgetfulness and night
> Shall spare thy fame, when in some larger day
> Of knowledge yet undream'd, Time makes a prey
> Of many a deed and name that once were bright.
> Thou, without haste or pause, from youth to age,
> Hast moved with sure steps to thy goal. And thine
> That sure renown which sage confirms to sage,
> Borne from afar. Yet wisdom shows a sign
> Greater, through all thy life, than glory's wage;
> Thy strength hath rested on the Love Divine.

The rest of the article is organized as follows. In §2, the fluid drag on a particle is described. The legacy of Stokes, highlighting the drag coefficient, is presented in §3. A particle's motion falling through a fluid is furnished in §4. The response of terminal fall velocity to key factors is delineated in §5. In §6, the impact of terminal fall velocity on fluvial hydraulics is summarized. Finally, an innovative perspective is delivered as the future research scope, highlighting open questions, in §7.

2. Description of fluid drag

From the fundamental principle, the fluid drag F_D acting on the interface between a fluid and a particle is defined as the component of the fluid force in the flow direction (figure 3). The fluid drag comprises skin friction drag and pressure drag. Therefore, fluid drag F_D is expressed as

$$F_D = -\int_S \tau_0 \sin\theta \,\mathrm{d}S - \int_S p\cos\theta \,\mathrm{d}S, \tag{2.1}$$

where τ_0 is the wall shear stress, p is the pressure intensity and S is the surface area of the particle.

(a) Stokes drag

(i) Creeping flow past a spherical particle

It is important to shed light on the Stokes drag that arises in a creeping flow, also called the *Stokes flow*, with a free stream velocity U past a spherical particle of diameter d (figure 3). Under such circumstances, the particle Reynolds number $\mathscr{R}$ $(= Ud/\nu)$ is quite small ($\mathscr{R} < 1$). Although derivation of the Stokes drag is given in standard textbooks of fluid mechanics, it has been found that there remains confusion in some of the derivational steps. The reasons for this are twofold:

- improper distinction between the Laplace operator and the H operator (details are given below);
- inaccurate derivation of the final form of the differential equation for the Stokes stream function.

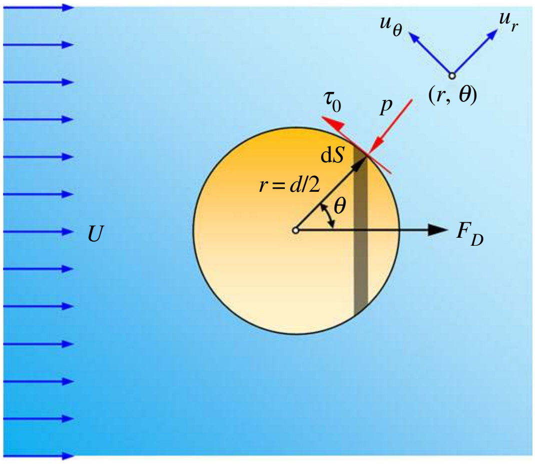

Figure 3. Schematic of fluid drag on a particle. (Online version in colour.)

Therefore, to take away such confusion, we put into focus the appropriate derivation of the Stokes drag, in brief, for clear understanding. The Navier–Stokes equations read

$$\frac{\partial \mathbf{u}}{\partial t} + (\mathbf{u} \cdot \nabla)\mathbf{u} = -\frac{1}{\rho_f}\nabla p + \nu \nabla^2 \mathbf{u} + \mathbf{f}, \tag{2.2}$$

where $\mathbf{u}$ is the velocity field and $\mathbf{f}$ is the body force vector per unit mass of fluid. Since $\mathscr{R} < 1$, the inertia terms $(\mathbf{u} \cdot \nabla)\mathbf{u}$ in equation (2.2) can be readily overlooked. In addition, for an incompressible fluid, $\nabla \cdot \mathbf{u} = 0$. Therefore, the identity $\nabla \times (\nabla \times \mathbf{u}) = \nabla(\nabla \cdot \mathbf{u}) - \nabla^2 \mathbf{u}$ makes $\nabla \times \boldsymbol{\Omega} = -\nabla^2 \mathbf{u}$, where $\boldsymbol{\Omega}$ is the vorticity vector ($= \nabla \times \mathbf{u}$). Under steady-state conditions and in the absence of any external body force ($\mathbf{f} = 0$), equation (2.2) produces

$$\nabla p = \mu \nabla^2 \mathbf{u} = -\mu \nabla \times \boldsymbol{\Omega}. \tag{2.3}$$

A spherical polar coordinate system (r, θ, ϕ) can now be sought to solve the problem (figure 3). The continuity equation reads

$$\nabla \cdot \mathbf{u} = \frac{1}{r^2}\frac{\partial}{\partial r}(r^2 u_r) + \frac{1}{r\sin\theta}\frac{\partial}{\partial \theta}(u_\theta \sin\theta) + \frac{1}{r\sin\theta}\frac{\partial u_\phi}{\partial \phi} = 0, \tag{2.4}$$

where (u_r, u_θ, u_ϕ) are the velocity components in (r, θ, ϕ). The axial symmetry suggests $u_\phi = \partial(\cdot)/\partial\phi = 0$. Therefore, the velocity components (u_r, u_θ) can be expressed with the aid of the *Stokes stream function* ψ as follows:

$$u_r = \frac{1}{r^2 \sin\theta}\frac{\partial \psi}{\partial \theta} \quad \text{and} \quad u_\theta = -\frac{1}{r\sin\theta}\frac{\partial \psi}{\partial r}. \tag{2.5}$$

Since the velocity field is axisymmetric, only the axial component of vorticity exists. The vorticity Ω_ϕ about the ϕ axis is expressed as

$$\Omega_\phi = \frac{1}{r}\left[\frac{\partial}{\partial r}(r u_\theta) - \frac{\partial u_r}{\partial \theta}\right] = -\frac{1}{r\sin\theta}H^2\psi \implies H^2 = \frac{\partial^2}{\partial r^2} + \frac{\sin\theta}{r^2}\frac{\partial}{\partial\theta}\left(\frac{1}{\sin\theta}\frac{\partial}{\partial\theta}\right). \tag{2.6}$$

Using equations (2.6), (2.3) produces

$$\frac{\partial p}{\partial r} = \frac{\mu}{r^2 \sin\theta}\frac{\partial}{\partial\theta}(H^2\psi) \quad \text{and} \quad \frac{\partial p}{\partial \theta} = -\frac{\mu}{\sin\theta}\frac{\partial}{\partial r}(H^2\psi). \tag{2.7}$$

From (2.7), eliminating the pressure term, one finds

$$H^4\psi = \left[\frac{\partial^2}{\partial r^2} + \frac{\sin\theta}{r^2}\frac{\partial}{\partial\theta}\left(\frac{1}{\sin\theta}\frac{\partial}{\partial\theta}\right)\right]^2 \psi = 0. \tag{2.8}$$

Equation (2.8) reveals that the Stokes stream function is bi-harmonic. The boundary conditions associated with the physical system are given as follows: (i) no slip at the surface of the particle and (ii) free stream velocity U far away from the particle. The first boundary condition suggests

$$\left.\frac{\partial\psi}{\partial r}\right|_{r=d/2} = \left.\frac{\partial\psi}{\partial\theta}\right|_{r=d/2} = 0. \tag{2.9}$$

Regarding the second boundary condition, we note that, far away from the particle ($r \to \infty$), the velocity components can be expressed as $u_r = U\cos\theta$ and $u_\theta = -U\sin\theta$. Using equation (2.5), this boundary condition produces

$$\psi|_{r\to\infty} = \frac{Ur^2}{2}\sin^2\theta. \tag{2.10}$$

Equation (2.10) provides the bottom line to search for the solution of ψ as $\psi(r,\theta) = f(r)\sin^2\theta$. Substituting this form of ψ into equation (2.6) produces

$$H^2 = \left(\frac{\mathrm{d}^2}{\mathrm{d}r^2} - \frac{2}{r^2}\right) f(r)\sin^2\theta = g(r)\sin^2\theta. \tag{2.11}$$

Using equation (2.11), equation (2.8) produces

$$H^4 = \left(\frac{\mathrm{d}^2}{\mathrm{d}r^2} - \frac{2}{r^2}\right) g(r)\sin^2\theta = \left(\frac{\mathrm{d}^2}{\mathrm{d}r^2} - \frac{2}{r^2}\right)^2 f(r)\sin^2\theta = 0. \tag{2.12}$$

With the substitution of $f(r) = r^q$ (q is an exponent), equation (2.12) becomes a quartic equation of q with roots $q = -1, 1, 2$ and 4. Therefore, ψ is expressed as

$$\psi = (a_1 r^{-1} + a_2 r + a_3 r^2 + a_4 r^4)\sin^2\theta, \tag{2.13}$$

where a_{1-4} are the coefficients. We note that this form of ψ is compatible with equation (2.10) if $a_3 = U/2$ and $a_4 = 0$. Using equation (2.9), the coefficients a_1 and a_2 are obtained as $a_1 = Ud^3/32$ and $a_2 = -3Ud/8$. Therefore, the final result is

$$\psi(r,\theta) = \frac{Ud^2}{16}\sin^2\theta\left(\frac{d}{2r} - \frac{6r}{d} + \frac{8r^2}{d^2}\right). \tag{2.14}$$

The terms in equation (2.14) are recognized as a *doublet*, a *Stokeslet* and a *uniform stream*, respectively. Among these terms, only the Stokeslet contributes to the vorticity. The velocity components and pressure, obtained from equations (2.5) and (2.7), respectively, are expressed as

$$u_r = U\cos\theta\left(1 + \frac{d^3}{16r^3} - \frac{3d}{4r}\right) \quad \text{and} \quad u_\theta = U\sin\theta\left(-1 + \frac{d^3}{32r^3} + \frac{3d}{8r}\right) \tag{2.15a}$$

and

$$p = p_0 - \frac{3\mu dU}{4r^2}\cos\theta, \tag{2.15b}$$

where p_0 is the uniform free stream pressure.

The shear stress $\tau_{r\theta}$ can be expressed as

$$\tau_{r\theta} = \mu\left(\frac{1}{r}\frac{\partial u_r}{\partial\theta} + \frac{\partial u_\theta}{\partial r} - \frac{u_\theta}{r}\right) = -\mu U\frac{\sin\theta}{r}\frac{3d^3}{16r^3}. \tag{2.16}$$

Therefore, the total drag (sum of skin friction drag and pressure drag) can be obtained from equation (2.1) with $\mathrm{d}S = (\pi d^2 \sin\theta\,\mathrm{d}\theta)/2$ (figure 3). The fluid drag F_D, called the Stokes drag, is

royalsocietypublishing.org/journal/rspa Proc. R. Soc. A 475: 20190277

given by

$$F_D = \underbrace{-\int_0^{\pi} \tau_{r\theta}|_{r=d/2} \sin\theta \, \mathrm{d}S}_{2\pi\mu Ud} \underbrace{- \int_0^{\pi} p|_{r=d/2} \cos\theta \, \mathrm{d}S}_{\pi\mu Ud} = 3\pi\mu Ud. \tag{2.17}$$

Equation (2.17) is known as Stokes' law, where the viscous shear force and pressure force contribute two-thirds and one-third, respectively.

(ii) Creeping flow past a long circular cylinder: Stokes' paradox

Interestingly, in a two-dimensional (2D) configuration, creeping flow past an object produces the *Stokes' paradox*. This paradox states:

> There remains no steady solution of the 2D Stokes equations that govern flow past an infinitely long circular cylinder.

In fact, with reference to a cylindrical polar coordinate system, the 2D Stokes stream function ψ (symbol remains the same for brevity) produces the following equation:

$$\nabla^4\psi = 0. \tag{2.18}$$

The solution of equation (2.18) can be set as $\psi(r,\theta) = f(r)\sin\theta$. Therefore, one obtains

$$\left(\frac{\mathrm{d}^2}{\mathrm{d}r^2} + \frac{1}{r}\frac{\mathrm{d}}{\mathrm{d}r} - \frac{1}{r^2}\right)^2 f(r) = 0. \tag{2.19}$$

The solution of $f(r)$ can be sought as

$$f(r) = b_1 r^{-1} + b_2 r + b_3 r \ln r + b_4 r^3, \tag{2.20}$$

where b_{1-4} are the coefficients. The boundary condition at infinity requires $b_3 = b_4 = 0$, while the no slip at the surface of the cylinder yields $b_1 = b_2 = 0$. This implies a vanishing flow field ($\mathbf{u} = 0$), suggesting the delicate role that the dimension plays in fluid dynamics.

(b) Newton drag

From the fundamental tenet, the *Newton drag*, for which drag coefficient C_D is constant, is expressed as a function of the dynamic pressure. It reads

$$F_D = C_D \tfrac{1}{2} \rho_f \bar{U}^2 A, \tag{2.21}$$

where $\bar{U}$ is the mean velocity received by the projected area A of the particle ($= \pi d^2/4$ for a spherical particle). The drag coefficient C_D must be determined experimentally.

3. The legacy of Stokes: a glance at the drag coefficient

Figure 4 illustrates the experimental data of the drag coefficient C_D of spheres, natural grains and shell fragments over a rich spectrum of particle Reynolds number $\mathscr{R}$ $(= w_t d/\nu)$ [8–17]. Three major realms are highlighted. They are the *Stokesian*, *transitional* and *Newtonian* realms. To be specific, Newton's law declares C_D to be a constant. This is expected to be true when the particle Reynolds number $\mathscr{R}$ is quite large, preferably more than 10^3 (figure 4). However, for $\mathscr{R} < 10^3$, C_D remains invariably a function of $\mathscr{R}$. In essence, balancing equations (2.17) and (2.21) yields the following relationship in the Stokesian realm:

$$C_D(\mathscr{R} < 1) = \frac{24}{\mathscr{R}}. \tag{3.1}$$

Equation (3.1) shows a drastic reduction of the drag coefficient with particle Reynolds number (also see figure 4). However, as the particle Reynolds number gradually exceeds unity, Stokes' law departs from the experimental data (see dotted line in figure 4).

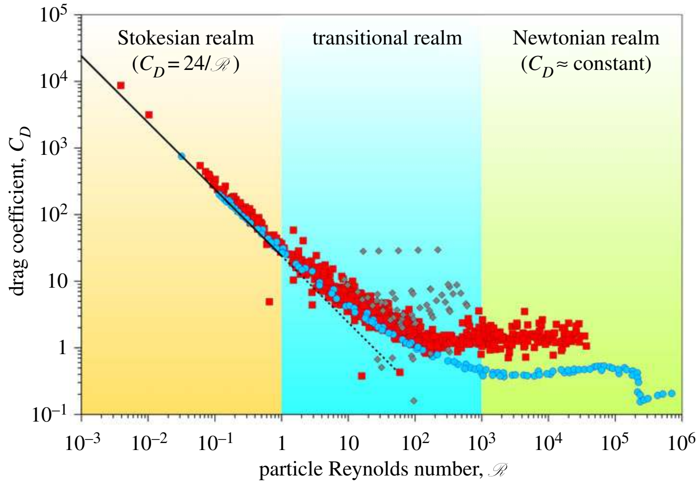

Figure 4. Drag coefficient C_D versus particle Reynolds number $\mathscr{R}$. Experimental data taken from several studies [8–17] include spheres (circle), natural grains (squares) and shell fragments (diamonds). The solid line is Stokes' law, while the dotted line is that extended to the transitional realm. (Online version in colour.)

Although Newton's and Stokes' laws work perfectly fine within their respective realms, there remains insufficient theoretical underpinning in bridging the apparent gap between these realms (figure 4). To this end, empirical formulations have played a promising role in capturing the transitional realm that lies between the Stokesian and Newtonian realms. In the following, we highlight the legacy of Stokes from two broad perspectives: theoretical and empirical formulations.

(a) Theoretical formulations

(i) Whitehead's contribution

Since Stokes' solution was obtained solely in the limit of $\mathscr{R} < 1$, Whitehead [18] attempted to improve the solution beyond $\mathscr{R} < 1$, considering higher approximations to the flow. Whitehead [18] applied a lower order approximation to determine the inertia terms in the Navier–Stokes equations, leading to an iterative technique. The boundary conditions at every iteration stage were independent of $\mathscr{R}$. Therefore, this technique turned out to be an expansion of the flow variables in powers of $\mathscr{R}$. However, such an assumption was not valid in the case of free stream flows. In fact, Whitehead [18] found that the second approximation to the flow velocity past a spherical particle became finite at infinity. This was an incompatible condition. In addition, it was identified that higher approximations to the flow velocity did not converge at infinity. Therefore, the expansion technique in powers of $\mathscr{R}$ created a situation where all terms but the leading one do not satisfy the boundary conditions. This phenomenon is known as *Whitehead's paradox*.

(ii) Oseen's contribution

Both Stokes' and Whitehead's paradoxes were resolved by Oseen [19,20]. He recognized that, far away from the sphere, the inertia force may not be trivial as compared with the viscous force. The viscous force can be predominant only if the disturbance decays faster in an exponential way. Stokes' theory was thus identified as self-inconsistent in the far field. Oseen [19,20] provided an improvement of the Stokes drag by partly considering the inertia terms in the Navier–Stokes equations. In essence, away from the sphere, the inertia terms $(\mathbf{u} \cdot \nabla)\mathbf{u}$ in equation (2.2) cannot be readily neglected, because the velocity field is almost spatially invariant there. It follows that the

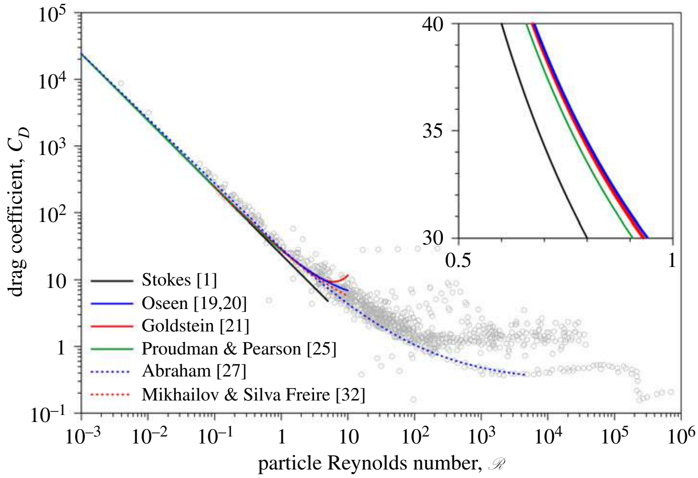

Figure 5. Drag coefficient C_D versus particle Reynolds number $\mathscr{R}$, obtained from the theoretical formulations, and the experimental data. (Online version in colour.)

effects of friction are negligible and, therefore, the inertia force becomes larger than the viscous force. However, taking into consideration the terms $(\mathbf{u} \cdot \nabla)\mathbf{u}$ in the governing equation, the mathematical analysis becomes too intricate to produce any straightforward analytical solution. Therefore, the solution is sought by expanding the stream function with respect to the particle Reynolds number. It is important to mention that the Stokes expansion is applied to the close field, while the Oseen expansion is used in the far field. Oseen [19,20] expressed the stream function as

$$\psi(r,\theta) = \frac{Ud^2}{16}\sin^2\theta\left(\frac{d}{2r} + \frac{8r^2}{d^2}\right) - \frac{3}{4}Ud^2\frac{1+\cos\theta}{\mathscr{R}}\left\{1 - \exp\left[-\mathscr{R}\frac{r}{2d}(1-\cos\theta)\right]\right\}. \tag{3.2}$$

Equation (3.2) satisfies the steady Navier–Stokes equations without external force to introduce body force and the appropriate boundary conditions at infinity. Moreover, close to the spherical surface (when r approaches $2d$), equation (3.2) recovers the Stokes stream function (see equation (2.14)). The drag coefficient was found to be

$$C_D(\mathscr{R} \le 1) = \frac{24}{\mathscr{R}}\left(1 + \frac{3}{16}\mathscr{R}\right). \tag{3.3}$$

Figure 5 illustrates the drag coefficient C_D as a function of particle Reynolds number $\mathscr{R}$, obtained from some of the theoretical formulae, and the experimental data of spheres, natural grains and shell fragments. Figure 5 shows that equation (3.3) has a good matching with the experimental data up to $\mathscr{R} = 10$.

(iii) Goldstein's contribution

Goldstein [21] gave an extended series solution of Oseen's approximation. It is

$$C_D(\mathscr{R} \le 2) = \frac{24}{\mathscr{R}}\left(1 + \frac{3}{16}\mathscr{R} - \frac{19}{1280}\mathscr{R}^2 + \frac{71}{20\,480}\mathscr{R}^3 - \frac{30\,179}{34\,406\,400}\mathscr{R}^4 + \frac{122\,519}{550\,502\,400}\mathscr{R}^5 - \cdots\right). \tag{3.4}$$

Equation (3.4) is plotted in figure 5. It appears that, for $\mathscr{R} > 2$, Goldstein's solution departs from the experimental data. Later, the last denominator within parenthesis on the right-hand side of equation (3.4) was corrected as 550 502 400. However, with regard to the above expansion, Goldstein [22] reported that, after the first two terms within the parenthesis, the drag coefficient obtained from the expansion of the Navier–Stokes equations would produce a different result from that given by equation (3.4).

(iv) Tomotika & Aoi's contribution

On the basis of Goldstein's approach and Oseen's approximations, Tomotika & Aoi [23] approximately expressed the Stokes stream function for small $\mathscr{R}$ ($\mathscr{R} < 1$) as

$$\psi(r,\theta) = -\frac{Ud^2}{4}\sin^2\theta\left[\frac{3}{4}\left(\frac{2r}{d}-\frac{d}{2r}\right)-\left(\frac{1}{2}+\frac{3}{32}\mathscr{R}\right)\left(\frac{4r^2}{d^2}-\frac{d}{2r}\right)+\frac{3}{32}\mathscr{R}\left(\frac{4r^2}{d^2}-\frac{d^2}{4r^2}\right)\cos\theta\right]. \tag{3.5}$$

In the limit $\mathscr{R} \to 0$, equation (3.6) produces the Stokes stream function (see equation (2.14)). They also reported that, whatever the values of $\mathscr{R}$ ($\mathscr{R} < 1$), the skin friction drag and pressure drag contribute two-thirds and one-third to the total drag, respectively.

(v) Stewartson's contribution

Stewartson [24] applied Oseen's linearized approximations to study the viscous flow past a sphere for large $\mathscr{R}$. It was reported that on the stoss side of the sphere a boundary layer is formed, whereas on the leeside a wake extends to infinity. The drag coefficient for large $\mathscr{R}$ ($\mathscr{R} \to \infty$) was found to be $C_D \approx 1.06$.

(vi) Proudman & Pearson's contribution

Proudman & Pearson [25] argued that the resulting solution for $\mathscr{R} < 1$, obtained from the expansion of the Navier–Stokes equations, is somewhat complicated, involving logarithms and powers of $\mathscr{R}$. They obtained the drag coefficient C_D as (also see figure 5)

$$C_D(\mathscr{R} < 1) = \frac{24}{\mathscr{R}}\left[1+\frac{3}{16}\mathscr{R}+\frac{9}{160}\mathscr{R}^2\log\frac{\mathscr{R}}{2}+\mathcal{O}(\mathscr{R}^2)\right]. \tag{3.6}$$

(vii) Chester *et al.*'s contribution

Chester *et al*. [26] extended the analysis of Proudman & Pearson [25] for $\mathscr{R} < 1$ up to the order of $\mathscr{R}^3 \log \mathscr{R}$ and expressed the drag coefficient C_D as

$$C_D(\mathscr{R} < 1) = \frac{24}{\mathscr{R}}\left[1+\frac{3}{16}\mathscr{R}+\frac{9}{160}\mathscr{R}^2\left(\gamma-\frac{323}{360}+\frac{5}{3}\log 2+\log\frac{\mathscr{R}}{2}\right)+\frac{27}{640}\mathscr{R}^3\log\frac{\mathscr{R}}{2}+\mathcal{O}(\mathscr{R}^3)\right], \tag{3.7}$$

where γ is the Euler–Mascheroni constant.

(viii) Abraham's contribution

Abraham [27] determined the fluid drag on a particle considering two distinct flow zones. In the external zone a frictionless flow was assumed, while in the internal zone a boundary layer flow was considered. The drag coefficient C_D was expressed as (also see figure 5)

$$C_D(0 < \mathscr{R} < 5000) = \left[0.5407+\left(\frac{24}{\mathscr{R}}\right)^{1/2}\right]^2. \tag{3.8}$$

(ix) van Dyke's contribution

van Dyke [28] extended the Goldstein's expansion to 24 terms in powers of $\mathscr{R}$. The drag coefficient C_D was expanded as

$$C_D = \frac{24}{\mathscr{R}} \sum_{n=0} c_n \left(\frac{\mathscr{R}}{4}\right)^n, \tag{3.9}$$

where c_n are the coefficients, given by van Dyke [28]. The results produced four significant figures ($C_D = 5.929$) at $\mathscr{R} = 3$ and one significant figure ($C_D = 5$) at $\mathscr{R} = 4$. The series solution was capable of capturing at least one more significant figure for $\mathscr{R}$ up to 50. For $\mathscr{R} \to \infty$, Stewartson's [24] result was recovered ($C_D \approx 1.06$).

(x) Hunter & Lee's contribution

Hunter & Lee [29] obtained 66 terms in the Goldstein series and sought the performance of $C_D(\mathscr{R})$ for $\mathscr{R} \to \infty$. However, neither Padé approximates nor Euler transformation applied to the solution gave good convergence. The asymptotic performance of $C_D(\mathscr{R})$ was found to follow $C_D(\mathscr{R}) - C_D(\mathscr{R} \to \infty) \propto \mathscr{R}^{-2/3}$ for $\mathscr{R} \to \infty$. Similar observation was also reported by van Dyke [26].

(xi) Weisenborn & Bosch's contribution

Weisenborn & Bosch [30] analytically determined the Oseen drag coefficient for $\mathscr{R} \to \infty$. They applied the induced forces method, which allowed the determination of a series of rational coefficients that converged to a suitable value for the drag coefficient. With the aid of the Shanks transformation in accelerated form, the drag coefficient was found to be $C_D \approx 1.058$.

(xii) Liao's contribution

Liao [31] applied the homotopy analysis method through which Whitehead's paradox could be easily resolved. The analytic approximations were able to capture the entire flow field, because the same approximations were applied to analyse the near and far flow field. The drag coefficient was derived at the 10th order of analytic approximation. Liao [31] expressed the drag coefficient C_D as

$$C_D(\mathscr{R} < 30) = \frac{24}{\mathscr{R}}(1 + 0.14\mathscr{R}^{0.7}) \left(1 + \sum_{q=1}^{\varpi(m,0)} \sum_{l=2q}^{m} k_m^{q,l} \mathscr{R}^{2q} \hbar^l \right), \tag{3.10}$$

where $k_m^{q,l}$ are constant coefficients, $\varpi(m,n)$ was defined as 'taking the integer part of $(m-n)/2$' and $\hbar$ is an auxiliary parameter.

(xiii) Mikhailov & Silva Freire's contribution

Mikhailov & Silva Freire [32] applied a generalized Shanks transformation to the Goldstein series (equation (3.4)) to precisely approximate the drag coefficient and to increase the convergence range. The Shanks transformation of equation (3.4) was obtained as

$$C_D(0.1 < \mathscr{R} < 10) = \frac{1920(3696 + 1665\mathscr{R} + 136\mathscr{R}^2)}{\mathscr{R}(295\,680 + 77\,760\mathscr{R} + 689\mathscr{R}^2)}. \tag{3.11}$$

Equation (3.12) is plotted in figure 5. However, with the help of experimental data, Mikhailov & Silva Freire [32] refined the coefficients in equation (3.11) and proposed the drag coefficient for $0.1 < \mathscr{R} < 1.183 \times 10^5$.

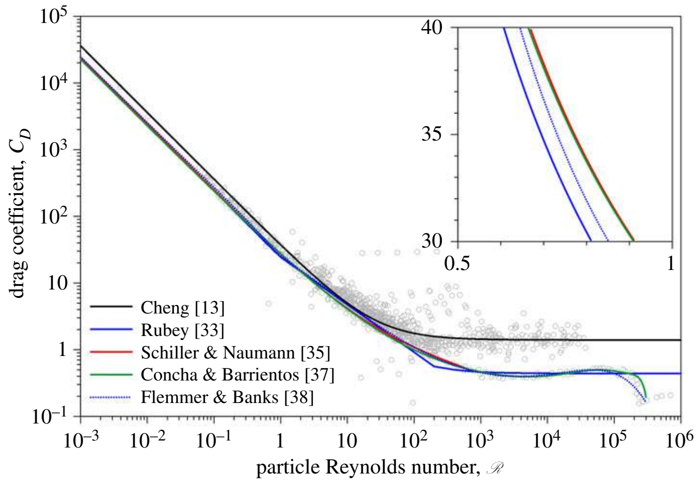

Figure 6. Drag coefficient C_D versus particle Reynolds number $\mathscr{R}$, obtained from the empirical formulations, and the experimental data. (Online version in colour.)

(b) Empirical formulations

A detailed compilation of some of the relevant empirical formulae of drag coefficient C_D is furnished below.

(i) Rubey

Rubey [33] found that the terminal fall velocity of finer particles, such as silt and fine sand, follows Stokes' law, whereas that of coarser particles, such as coarse sand, pebble and boulder, deviates from Stokes' law. Rubey [33] expressed the drag coefficient C_D as

$$C_D = \frac{A_1}{\mathscr{R}} + A_2, \tag{3.12}$$

where A_1 and A_2 are the phenomenological coefficients [33]. In essence, in the limit of infinite and small $\mathscr{R}$, this empirical law recovers Newton's and Stokes' laws, respectively. The above formula was introduced to determine the terminal fall velocity of natural particles, such as silt, sand and gravel. Figure 6 shows the drag coefficient C_D as a function of particle Reynolds number $\mathscr{R}$, obtained from some of the empirical formulae, and the experimental data of spheres, natural grains and shell fragments. Equation (3.12) is plotted in figure 6 for $A_1 = 24$ and $A_2 = 0.44$, as suggested by Guo [34].

(ii) Schiller & Naumann

Schiller & Naumann [35] introduced a three-constant formula for the drag coefficient. They expressed the drag coefficient C_D as (also see figure 6)

$$C_D(\mathscr{R} < 800) = \frac{24}{\mathscr{R}}(1 + 0.15\mathscr{R}^{0.687}). \tag{3.13}$$

(iii) Dou

Dou [36] sought trigonometric functions to express the drag coefficient. The drag coefficient C_D was obtained as

$$C_D(\mathscr{R} < 2 \times 10^5) = \frac{24}{\mathscr{R}}\left(1 + \frac{3}{16}\mathscr{R}\right)\cos^3\delta + 0.45\sin^2\delta, \tag{3.14}$$

where δ is given by $\delta(\mathscr{R} \le 0.5) = 0$, $\delta(0.5 < \mathscr{R} < 2500) = \pi \ln(2\mathscr{R})/[2\ln(5000)]$ and $\delta(\mathscr{R} \ge 2500) = \pi/2$.

(iv) Concha & Barrientos

Concha & Barrientos [37] argued that a fifth-order polynomial could be used to represent the drag coefficient over a wide range of particle Reynolds number. They obtained the drag coefficient C_D as (also see figure 6)

$$C_D(\mathscr{R} < 3 \times 10^5) = 0.284153\left(1 + \frac{9.04}{\mathscr{R}^{1/2}}\right)^2 \sum_{j=0}^{5} a_j \mathscr{R}^j, \tag{3.15}$$

where the coefficients a_j can be approximately expressed as $a_0 = 0.962$, $a_1 = 2.736 \times 10^{-5}$, $a_2 = -3.938 \times 10^{-10}$, $a_3 = 2.476 \times 10^{-15}$, $a_4 = -7.159 \times 10^{-21}$ and $a_5 = 7.437 \times 10^{-27}$.

(v) Flemmer & Banks

Using experimental data, Flemmer & Banks [38] expressed the drag coefficient C_D as (also see figure 6)

$$C_D(\mathscr{R} < 3 \times 10^5) = \frac{24}{\mathscr{R}} 10^{\lambda} \quad \text{and} \quad \lambda = 0.261\mathscr{R}^{0.369} - 0.105\mathscr{R}^{0.431} - \frac{0.124}{1 + \log^2 \mathscr{R}}. \tag{3.16}$$

(vi) Turton & Levenspiel

Turton & Levenspiel [39] proposed a five-constant formula for the drag coefficient as

$$C_D(\mathscr{R} < 2 \times 10^5) = \frac{24}{\mathscr{R}}(1 + 0.173\mathscr{R}^{0.657}) + \frac{0.413}{1 + 16300\mathscr{R}^{-1.09}}. \tag{3.17}$$

(vii) Cheng

Cheng [13] reported the following relationship to calculate the terminal fall velocity of sediment particles as a generalization of Rubey's [33] formula, equation (3.12):

$$C_D = \left[\left(\frac{A_1}{\mathscr{R}}\right)^{1/A_3} + A_2^{1/A_3}\right]^{A_3}, \tag{3.18}$$

where the coefficients A_1 and A_2 and the exponent A_3 were reported in the literature [6]. In the above, the particle Reynolds number is obtained as $\mathscr{R} = w_t d_n/\nu$, where d_n is the nominal diameter of sediment particles of median size d. It is approximately taken as $d_n = d/0.9$ [6]. Equation (3.18) is plotted in figure 6 for $A_1 = 36$, $A_2 = 1.4$ and $A_3 = 1$, as suggested by Fredsøe & Deigaard [40]. The resulting curve shows good agreement with the experimental data.

(viii) Ceylan *et al.*

Ceylan *et al.* [41] used an approximate series solution and expressed the drag coefficient C_D as

$$\begin{aligned} C_D(0.1 < \mathscr{R} < 2 \times 10^6) = 1 - 0.5\exp(0.182) + 10.11\mathscr{R}^{-2/3}\exp(0.952\mathscr{R}^{-1/4}) \\ - 0.03859\mathscr{R}^{-4/3}\exp(1.3\mathscr{R}^{-1/2}) + 0.037 \times 10^{-4}\mathscr{R}\exp(-0.125 \times 10^{-4}\mathscr{R}) \\ - 0.116 \times 10^{-10}\mathscr{R}^2\exp(-0.444 \times 10^{-5}\mathscr{R}). \end{aligned} \tag{3.19}$$

(ix) Brown & Lawler

Considering a large experimental dataset, Brown & Lawler [42] applied the wall correction to the data points that emerged from terminal fall velocity measurements for cylinders. To apply the wall correction, they used the results of Fidleris & Whitmore [43]. They recommended the following equation to estimate the drag coefficient C_D:

$$C_D(\mathscr{R} < 2\times 10^5) = \frac{24}{\mathscr{R}}(1+0.15\mathscr{R}^{0.681}) + \frac{0.407}{1+8710\mathscr{R}^{-1}}. \tag{3.20}$$

(x) Almedeij

Almedeij [44] applied a matched asymptotic approach, where a wide trend of the drag coefficient was divided into smaller segments. These segments were combined together to form a final relationship of drag coefficient. The drag coefficient C_D was expressed as

$$C_D(\mathscr{R} < 10^6) = \left[\frac{1}{(\zeta_1+\zeta_2)^{-1}+\zeta_3^{-1}} + \zeta_4\right]^{1/10}, \tag{3.21a}$$

where ζ_{1-4} are functions of $\mathscr{R}$. They are expressed as

$$\left.\begin{aligned} \zeta_1 &= \left(\frac{24}{\mathscr{R}}\right)^{10} + \left(\frac{21}{\mathscr{R}^{0.67}}\right)^{10} + \left(\frac{4}{\mathscr{R}^{0.33}}\right)^{10} + 0.4^{10}, \quad \zeta_2 = \frac{1}{0.5^{-10}+(0.148\mathscr{R}^{0.11})^{-10}},\\ \zeta_3 &= \left(\frac{1.57\times 10^8}{\mathscr{R}^{1.625}}\right)^{10} \quad \text{and} \quad \zeta_4 = \frac{1}{0.2^{-10}+(6\times 10^{-17}\mathscr{R}^{2.63})^{-10}}. \end{aligned}\right\} \tag{3.21b}$$

(xi) Cheng

Cheng [45] used the experimental data of Brown & Lawler [42] and expressed the drag coefficient C_D as

$$C_D(2\times 10^{-3} < \mathscr{R} < 2\times 10^5) = \frac{24}{\mathscr{R}}(1+0.27\mathscr{R})^{0.43} + 0.47[1-\exp(-0.04\mathscr{R}^{0.38})]. \tag{3.22}$$

On the right-hand side of the above equation, the first term signifies the extended Stokes' law that was found to be applicable for $\mathscr{R} < 100$. In addition, the second term denotes an exponential function that takes into account the deviations from Newton's law. In this regard, it is worth mentioning that Yang *et al*. [46] obtained a series of empirical formulae for the drag coefficient C_D based on the formulations of Stokes, Oseen and Goldstein. The fitting parameters were determined with the aid of experimental data.

In this context, it is pertinent to point out that Rouse [47] gave an empirical curve for the drag coefficient using the experimental data of spheres. However, except for Rubey's formula and its modified version (see equations (3.12) and (3.18), respectively), it has been found that the other empirical formulae do not vary significantly from each other, because most of them were prepared using the experimental data of spheres. These formulae do not take into account the experimental data of natural particles and shell fragments. Therefore, only some of the empirical formulae for spheres are plotted in figure 6. It may also be noted that, in the theoretical formulations, a regular spherical particle was considered. As a result, the theoretical predictions for the drag coefficient of spheres cannot be strictly applied to natural particles (figure 5).

4. Particle motion falling through a fluid

(a) Governing equation

The equation of motion of a spherical particle falling through a fluid is given by the *Boussinesq–Basset–Oseen* equation [34]. It is expressed as

$$(m_p+\alpha_m m_f)\frac{\mathrm{d}w}{\mathrm{d}t} = (m_p-m_f)g - C_D\frac{1}{2}\rho_f w^2\frac{\pi}{4}d^2 - \frac{3}{2}\pi^{1/2}\rho_f\nu^{1/2}d^2\int_0^t \frac{\mathrm{d}w}{\mathrm{d}\sigma}(t-\sigma)^{-1/2}\,\mathrm{d}\sigma, \tag{4.1}$$

where m_p and m_f are the mass of particle and fluid, respectively, α_m is the added mass coefficient, w is the fall velocity of the particle, t is the time, g is the acceleration due to gravity and σ is the dummy variable.

The terms appearing in equation (4.1) can be explained one by one. The term on the left-hand side denotes the particle inertia, including the added mass. The added mass is often introduced when an accelerating (or retarding) particle moves in a fluid. The reason is attributed to the fact that, since both the particle and fluid cannot possess the same space concurrently, the traversing particle moves with a finite volume of fluid surrounding it. It turns out that a finite volume of fluid is in motion with the particle. In practice, the assumption of $\alpha_m = 0.5$ is frequently sought. On the right-hand side of equation (4.1), the first term is the submerged weight of the particle, while the second term represents the fluid drag. In addition, the third term signifies the Basset force, which arises due to the particle acceleration as a result of unsteady viscous shear on the surface of the particle. In this context, it is worth noting that, in recent years, the settling of non-spherical particles falling through a fluid was studied by Yaghoobi & Torabi [48,49] and Dogonchi *et al.* [50].

(b) Equilibrium state

At the equilibrium state ($w \to w_t$), the inertia and the Basset terms disappear, and the particle achieves the terminal fall velocity. The terminal fall velocity w_t, from equation (4.1), can be expressed as

$$w_t = \left(\frac{4\Delta g d}{3C_D}\right)^{1/2}, \tag{4.2}$$

where Δ is the submerged relative density of the particle $[=(\rho_p - \rho_f)/\rho_f]$ and ρ_p is the mass density of the particle.

To solve equation (4.2), accurate expression for the drag coefficient C_D is to be used. However, using equation (3.18), which is applicable to natural particles, equation (4.2) becomes

$$w_t = \frac{A_1}{A_2}\frac{\nu}{d_n}\left\{\left[\frac{1}{4} + \left(\frac{4A_2}{3A_1^2}D_*^3\right)^{1/A_3}\right]^{1/2} - \frac{1}{2}\right\}^{A_3}, \tag{4.3}$$

where D_* is the particle parameter $[=d_n(\Delta g/\nu^2)^{1/3}]$.

In addition, several empirical formulae of the terminal fall velocity of natural particles are available in the literature. Hallermeier [12] considered three different ranges of particle parameter D_* (sand particles) and expressed the terminal fall velocity w_t as

$$w_t(D_* \le 3.42) = \frac{\nu}{d_n}\frac{D_*^3}{18}, \quad w_t(3.42 < D_* < 21.54) = \frac{\nu}{d_n}\frac{D_*^{2.1}}{6} \quad \text{and} \quad w_t(D_* \ge 21.54) = 1.05\frac{\nu}{d_n}D_*^{1.5}. \tag{4.4}$$

Analysing the experimental data, Dietrich [51] expressed the terminal fall velocity w_t of natural particles as

$$w_t = \frac{\nu}{d_n}10^{-1.25572+2.92944\log D_* - 0.29445\log^2 D_* - 0.05175\log^3 D_* + 0.01512\log^4 D_*}. \tag{4.5}$$

Ahrens [52] expressed the terminal fall velocity w_t of quartz sand particles as a function of particle parameter D_* as

$$w_t = \frac{\nu}{d_n}\{0.055D_*^3\tanh[12D_*^{-1.77}\exp(-4\times10^{-4}D_*^3)] + 1.06D_*^{1.5}\tanh[0.016D_*^{1.5}\exp(-120D_*^{-3})]\}. \tag{4.6}$$

Jiménez & Madsen [53] gave an empirical formula to simplify the long expression proposed by Dietrich [51]. In non-dimensional form, the terminal fall velocity w_t of natural particles was set as

$$W_* = \frac{w_t}{(\Delta g d_n)^{1/2}}, \quad W_* = \left(0.954 + \frac{20.48}{S_*}\right)^{-1} \quad \text{and} \quad S_* = d_n \frac{(\Delta g d_n)^{1/2}}{\nu}. \tag{4.7}$$

5. Response of the terminal fall velocity to key factors

(a) Effects of particle shape

Natural particles are hardly spherical. A large variety of non-spherical natural and artificial particles is used in engineering applications; for instance, disc [54], oblate spheroid [55], ice crystals [56], snowflakes [57,58], mineral dust [59], volcanic ash [60] and shell fragments as littoral sediments [15,17]. As a result, the particle shape is worth considering while estimating the drag coefficient and, in turn, the terminal fall velocity [17,61,62]. It was found that, for an irregular particle falling through a fluid, the most stable configuration of the particle corresponds to the maximum projected area in the direction of particle motion [63]. Therefore, as compared with a spherical particle of diameter d, an irregular particle possesses a larger surface area that displaces fluid around it, inducing larger skin friction drag and pressure drag for the same terminal fall velocity. For the same particle parameter, an irregular particle produces more surface curvature, giving rise to the drag coefficient because of the flow separation from the surface of the particle. Consequently, the terminal fall velocity drops down. In addition, the surface irregularity might induce instability to the particle, yielding rotation and vibration of the particle, which eventually reduces the terminal fall velocity.

It is worth highlighting that Mrokowska [54] studied specifically the effects of particle shape on a particle settling through a stratified fluid. In a two-layer fluid with a density transition, it was found that a disc exhibits five phases of settling. The orientation of the disc was observed to vary from horizontal to vertical with two local minimum values of disc velocity in the transition layer. It was also evidenced that particle settling is affected by the density difference, stratification strength and transition layer thickness. For non-spherical particles, Gustavsson *et al*. [64] reported that the orientation of settling particles can be predicted by applying a Gaussian distribution.

Researchers proposed shape factors in the empirical formulations in order to mimic the terminal fall velocity of an irregular particle [11,51,65,66]. Among many shape factors, the most commonly used is the Corey shape factor. It measures the cross-sectional area of a spherical particle relative to the maximum cross-sectional area of an ellipsoidal particle. The Corey shape factor S_p is expressed as $S_p = a_z/(a_x a_y)^{1/2}$, where a_x, a_y and a_z are the longest, intermediate and shortest axes of the particle. To be specific, S_p varies in the range $0 < S_p < 1$; for instance, $S_p \approx 0.7$ for naturally worn particles [6]. Another shape factor that might have some influence, although trivial, on the terminal fall velocity is the roundness factor P. It defines the mean radius of curvature of several edges of a particle to the radius of an inscribing circle covering the maximum projected area of the particle.

For quartz sand particles, Komar & Reimers [11] used equation (3.1) and expressed equation (4.2) as

$$w_t = \frac{d_n^2}{18\nu}\frac{\Delta g}{f(S_p)}, \quad f(0.4 \le S_p < 0.8) = 0.946 S_p^{-0.378} \quad \text{and} \quad f(S_p < 0.4) = 2.18 - 2.09 S_p. \tag{5.1}$$

Dietrich [51] found that, for coarse sand with a Corey shape factor $S_p = 0.7$ and a roundness factor $P = 3.5$, the terminal fall velocity is nearly 0.68 times that of a spherical particle with the same particle parameter D_*. For lower values of D_*, the reduction in terminal fall velocity owing to the Corey shape factor and roundness factor is insignificant. However, when the Corey shape factor remains small, a lower value of the roundness factor produces a smaller terminal fall velocity.

Wu & Wang [65] reported that the coefficients A_1, A_2 and the exponent A_3 in equation (4.3) are dependent on the Corey shape factor S_p. They obtained A_1, A_2 and A_3 as

$$A_1 = 53.5\exp(-0.65S_p), \quad A_2 = 5.65\exp(-2.5S_p) \quad \text{and} \quad A_3 = 0.7 + 0.9S_p. \tag{5.2}$$

On the other hand, Camenen [66] suggested that the coefficients A_1, A_2 and the exponent A_3 in equation (4.3) can be expressed as a function of the Corey shape factor S_p and roundness factor P. Using the experimental data of various researchers, Camenen [66] expressed A_1, A_2 and A_3 as

$$\left.\begin{aligned} A_1 &= 24 + 100\left[1 - \sin\left(\frac{\pi}{2}S_p\right)\right]^{2.1+0.06P}, \quad A_2 = 0.39 + 0.22(6-P) + 20\left[1 - \sin\left(\frac{\pi}{2}S_p\right)\right]^{1.75+0.35P} \\ \text{and} \quad A_3 &= 1.2 + 0.12P\sin^{0.47}\left(\frac{\pi}{2}S_p\right). \end{aligned}\right. \tag{5.3}$$

(b) Effects of hindered settling

It has been revealed experimentally that, in a fluid carrying suspended sediment particles, flow around contiguous falling particles causes a larger fluid drag than that in a clear fluid (without particles). This phenomenon is called the *hindered settling effect* [67]. As a consequence, terminal fall velocity w_{tc} in a sediment-laden fluid diminishes from that in a clear fluid. Richardson & Zaki [67] proposed the terminal fall velocity w_{tc} in a sediment-laden fluid as

$$w_{tc} = w_t(1-C)^{\vartheta}, \tag{5.4}$$

where w_t is the terminal fall velocity in a clear fluid, C is the sediment concentration and ϑ is the hindered settling exponent.

Figure 7*a* depicts the ratio of the terminal fall velocity in a sediment-laden fluid w_{tc} to the terminal fall velocity in a clear fluid w_t as a function of the sediment concentration C, obtained from the experimental observations [68–71]. The experimental data plots are almost confined to a shaded zone, whose extreme boundaries obey equation (5.4) and correspond to $\vartheta = 2.5$ and 6. In fact, the hindered settling exponent ϑ has been found to be dependent on the particle Reynolds number $\mathscr{R}$ [67]. The $\vartheta(\mathscr{R})$ relationship obtained by Richardson & Zaki [67] was approximated as follows [72]:

$$\left.\begin{aligned} &\vartheta(\mathscr{R} < 0.2) = 4.65, \quad \vartheta(0.2 < \mathscr{R} < 1) = 4.4\mathscr{R}^{-0.03} \\ \text{and} \quad &\vartheta(1 < \mathscr{R} < 500) = 4.4\mathscr{R}^{-0.1}, \quad \vartheta(\mathscr{R} > 500) = 2.4. \end{aligned}\right\} \tag{5.5}$$

On the other hand, Garside & Al-Dibouni [73] expressed the hindered settling exponent ϑ as

$$\vartheta = \frac{5.1 + 0.27\mathscr{R}^{0.9}}{1 + 0.1\mathscr{R}^{0.9}}. \tag{5.6}$$

In figure 7*b*, the experimental data of the hindered settling exponent ϑ are plotted as a function of particle Reynolds number $\mathscr{R}$ [68–71,74,75]. In addition, the $\vartheta(\mathscr{R})$ relationships proposed by Richardson & Zaki [67] and Garside & Al-Dibouni [73] are shown. Tomkins *et al.* [76] found the hindered settling exponent ϑ given by Richardson & Zaki [67] to be much larger for natural sand than for regular particles, as also evident from figure 7*b*. The effects of hindered settling are therefore quite large for natural particles. In essence, the effects of hindered settling become more promising for irregular particles. Tomkins *et al.* [76] reported that, for a sediment concentration of $C = 0.4$, the terminal fall velocity w_{tc} of fine and medium sands diminishes to approximately 70% of the estimation of w_{tc} from the available empirical formulae of ϑ.

Cheng [77] reported that the hindered settling exponent ϑ not only depends on the particle Reynolds number $\mathscr{R}$ but also on the sediment concentration C and the submerged relative

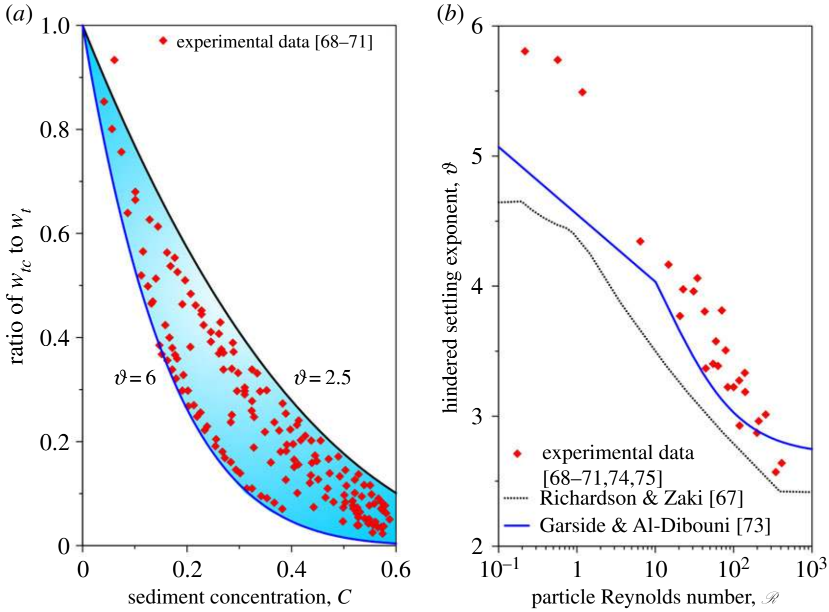

Figure 7. (*a*) Ratio of w_{tc} to w_t versus sediment concentration C and (*b*) hindered settling exponent ϑ versus particle Reynolds number $\mathscr{R}$. (Online version in colour.)

density Δ. He proposed that the hindered settling exponent ϑ can be obtained from the following equation:

$$(1-C)^{\vartheta} = 2\left(\frac{1-C}{2-3C}\right)\left\{\frac{\sqrt{\mathscr{R}^{2/3}(10+\mathscr{R}^{2/3})\left[(1/4)((1-C)(2-3C)^2/1+\Delta C)\right]^{2/3}+25}-5}{(25+\mathscr{R}^{4/3}+10\mathscr{R}^{2/3})^{1/2}-5}\right\}^{3/2}. \tag{5.7}$$

Figure 8*a*,*b* illustrates the variations of hindered settling exponent ϑ as a function of particle Reynolds number $\mathscr{R}$, obtained from equation (5.7), for different values of sediment concentration $C(=0.01,\ 0.05,\ 0.1$ and $0.5)$ and submerged relative density $\Delta(=0.5,\ 1,\ 1.65$ and $2.5)$. From figure 8*a*, it appears that, for $C \leq 1$, the $\vartheta(\mathscr{R})$ relationship is only sensitive for $\mathscr{R} < 1$ and $\mathscr{R} > 100$ (see the enlarged frames). In addition, figure 8*b* shows that, for a given particle Reynolds number $\mathscr{R}$, the hindered settling exponent ϑ increases as the submerged relative density Δ increases.

Using the experimental data, Oliver [78] reported the terminal fall velocity w_{tc} in a sediment-laden fluid as

$$w_{tc} = w_t(1-2.15C)(1-0.75C^{0.33}). \tag{5.8}$$

Sha [79] included the effects of median sediment size d_{50} in the formulation of w_{tc} and proposed the following formula:

$$w_{tc} = w_t\left(1-\frac{C}{2d_{50}^{1/2}}\right)^3. \tag{5.9}$$

Soulsby [80] suggested that the terminal fall velocity w_{tc} in a sediment-laden fluid could be calculated from equation (4.3) when A_1, A_2 and A_3 take the following forms:

$$A_1 = 26(1-C)^{-4.7}, \quad A_2 = 1.3(1-C)^{-4.7} \quad \text{and} \quad A_3 = 1. \tag{5.10}$$

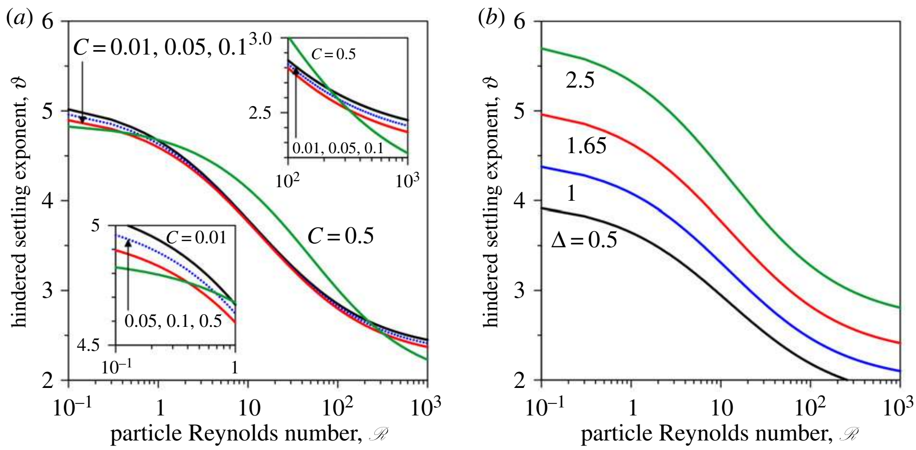

Figure 8. Hindered settling exponent ϑ versus particle Reynolds number $\mathscr{R}$ for different values of (*a*) sediment concentration C and (*b*) submerged relative density Δ. (Online version in colour.)

(c) Effects of turbulence

Experimental observations and numerical simulations of particle settling in homogeneous and isotropic turbulence with a vanishing mean flow velocity have evidenced that the turbulence is to enhance the terminal fall velocity [81–89]. However, a few studies reported that the terminal fall velocity reduces in moderately weak turbulence [90–92]. The direct numerical simulation has been applied to study the dynamics of particle settling in turbulence [84,92,93], especially with different volume fractions to study the effects of clustering [55,94,95]. Essentially, the effects of small-scale turbulence on particle motion are ascertained by the *Stokes number* $\mathcal{S}$. It signifies the ratio of particle relaxation time $t_p[=d^2(\rho_p - \rho_f)/(18\mu)]$ to Kolmogorov time scale $t_K[=(\nu/\varepsilon)^{1/2}]$, where ε is the turbulent kinetic energy dissipation rate. Therefore, the Stokes number $\mathcal{S}$ is expressed as

$$\mathcal{S} = \frac{t_p}{t_K} = \frac{\Delta}{18}\left(\frac{d}{\eta}\right)^2, \tag{5.11}$$

where η is the Kolmogorov length scale $[=(\nu^3/\varepsilon)^{1/4}]$. Wang *et al*. [96] found that, for $d/\eta \approx 0.5$, the terminal fall velocity was nearly equal to its value in a clear fluid. In addition, the terminal fall velocity was found to increase with an increase in Reynolds number based on the longitudinal turbulence intensity and the integral length scale. A reduction in terminal fall velocity was observed for $d/\eta < 0.5$, resulting from the retarding effect due to small-scale eddies. However, in relatively strong turbulence, the terminal fall velocity was found to increase considerably [91].

Nielsen [90] suggested that the effects of turbulence on terminal fall velocity are primarily governed by four key mechanisms, such as nonlinear drag, vortex tapping, fast tracking and the effects of loitering. They are discussed below.

(i) Nonlinear drag

Nonlinear fluid drag can cause a reduction in terminal fall velocity [90]. However, this is expected to be significant for coarser particles [96]. Nielsen [97] reported that the reduction w_{rt} in terminal fall velocity can be expressed as

$$|w_{rt}| = \frac{|w_t|}{16}\left(\frac{a_m}{g}\right)^2, \tag{5.12}$$

where a_m is the maximum fluid acceleration. For practical circumstances, the maximum fluid acceleration a_m is much smaller than the gravitational acceleration g (e.g. $a_m \approx 0.01g$). Therefore,

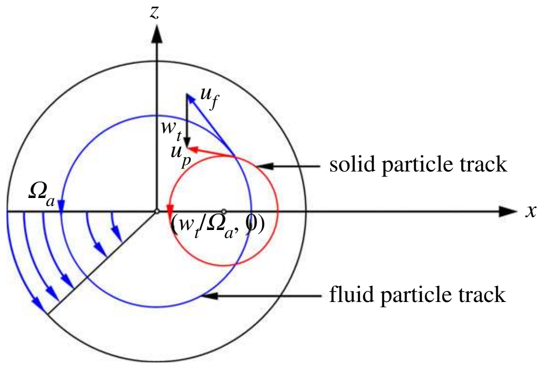

Figure 9. Schematic of vortex trapping. (Online version in colour.)

equation (5.12) suggests that the reduction w_{rt} in terminal fall velocity is $w_{rt} \approx 10^{-5} w_t$, which is trivial.

(ii) Vortex trapping

Forced vortices can trap particles, reducing their terminal fall velocity [98]. This phenomenon is quite common in a wide variety of processes in the realm of fluvial hydraulics; for instance, vortices formed in the leeside of bedforms create *surface boils* that carry sediment particles. These surface boils, trapping sediment particles in their core, eventually reach the free surface. In addition, sediment entrainment from a rippled bed under the action of waves is governed by the vortex trapping mechanism. Nielsen [97] assumed that the particle velocity u_p remains equal to the summation of flow velocity u_f and terminal fall velocity w_t, as sketched in figure 9. Under such an assumption, a particle, trapped in a forced vortex with an angular velocity Ω_a, can travel forever along any circle whose centre is located at $(w_t/\Omega_a, 0)$.

(iii) Fast tracking

Considerable difference in mass density or inertia yields a deviation in the particle track from the circular path. It turns out that the finer particles are curved inwards, while the coarser particles are curved outwards. As a consequence, finer particles remain trapped, whereas coarser particles try to escape as long as the vortices survive. Maxey & Corrsin [99] revealed an astonishing consequence of the outward curving, called *fast tracking* (figure 10). The finer particles are attracted along a fast track (see the dashed line in figure 10), which follows the right- and left-hand edges of clockwise and counter-clockwise vortices, respectively. In essence, the fast tracking mechanism enhances the terminal fall velocity by sweeping the particles towards a preferential direction.

(iv) Effects of loitering

The vortex trapping and fast tracking mechanisms become ineffective if the particles are too swift to be directed along the fast track or if the vortices are short-lived. As a result, the terminal fall velocity reduces, suggesting a retarding effect that can be modelled via the effects of loitering (figure 10). The crux of the effects of loitering is that a particle falling through a non-uniform velocity field spends more time with fluid, which flows opposite to the particle motion. Therefore, a coarser particle suffers from a retarding effect; for instance, the particle that falls along the vertical line of symmetry (figure 10). Nielsen [90] suggested that the effects of loitering become effective when the terminal fall velocity becomes 0.3 times larger than the longitudinal turbulence intensity. However, in homogeneous and isotropic turbulence, the effects of loitering play an insignificant role [92].

royalsocietypublishing.org/journal/rspa *Proc. R. Soc. A* **475**: 20190277

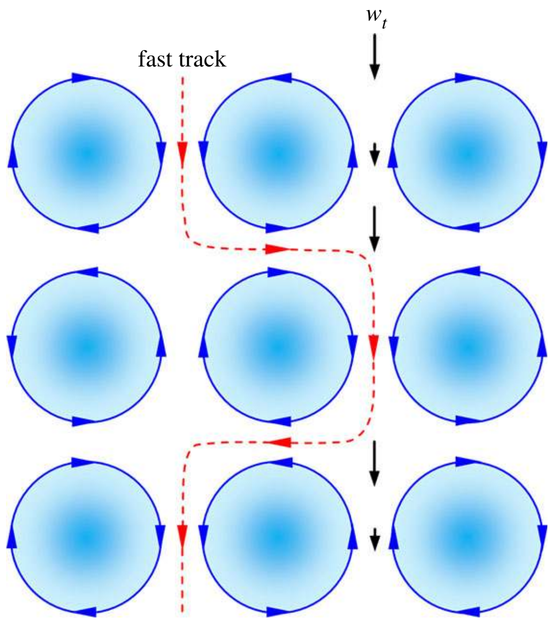

Figure 10. Schematic of fast tracking and the effects of loitering. (Online version in colour.)

6. Impact of the terminal fall velocity on fluvial hydraulics

In this section, the impact of terminal fall velocity on some key aspects of fluvial hydraulics is delineated. These are the hydrodynamics of sediment threshold, bedload transport and suspended load transport.

(a) Hydrodynamics of sediment threshold

The sediment threshold refers to a critical flow condition (commonly called the threshold condition) for which the bed shear stress is just adequate to entrain the surface sediment particles into the flow. It indicates that, at the threshold condition, the mean flow velocity U_f or the bed shear stress τ_b just reach their respective threshold values U_{fc} and τ_{bc}. The state-of-the-science of the bed sediment entrainment was recently reviewed elsewhere [100]. In essence, researchers attempted to correlate the threshold mean flow velocity U_{fc} or the threshold bed shear stress τ_{bc} with the terminal fall velocity w_t of sediment particles. Some of these attempts are furnished below.

Yang [101] used a force balance model considering the submerged weight F_G of the particle to be balanced by the fluid drag F_D of a falling particle, when the particle reaches the terminal fall velocity w_t. He obtained the following equation for the threshold mean flow velocity U_{fc}:

$$U_{fc} = w_t \left(\frac{\psi_1 \psi_2 \psi_3}{\psi_2 + \psi_3} \right)^{1/2} \left[1 + \frac{5.75}{B_R} \left(\log \frac{h}{d} - 1 \right) \right], \tag{6.1}$$

where ψ_{1-3} are phenomenological coefficients, B_R is the roughness function and h is the flow depth. However, to simplify the above equation, Yang [101] used ample experimental data and expressed the threshold mean flow velocity U_{fc} as

$$U_{fc}(0 < R_{*c} < 70) = w_t \left(0.66 + \frac{2.5}{\log R_{*c} - 0.06} \right) \quad \text{and} \quad U_{fc}(R_{*c} \geq 70) = 2.05 w_t, \tag{6.2}$$

where R_* is the shear Reynolds number ($= u_* k_s/\nu$), k_s is the roughness height and subscript 'c' refers to the threshold condition. For uniform sediments, roughness height can be taken approximately as the particle size ($k_s = d$).

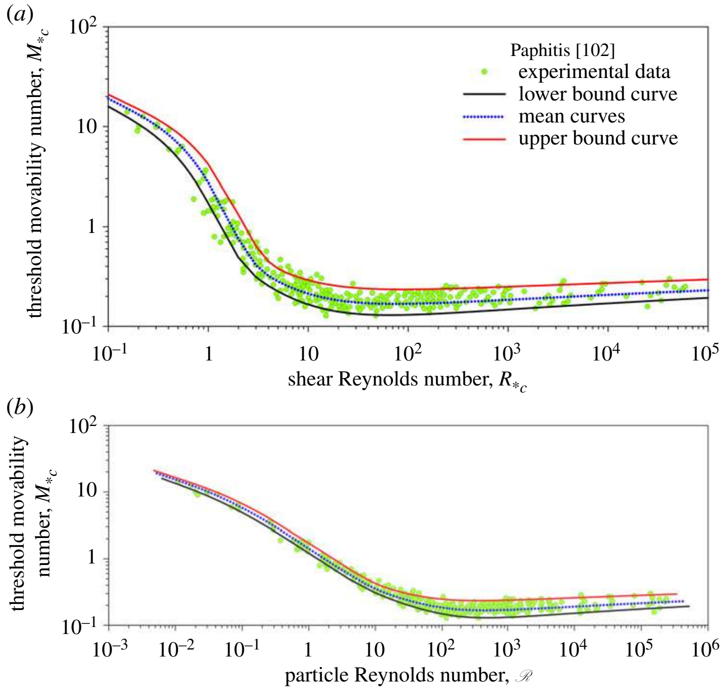

Figure 11. (*a*) Threshold movability number M_{*c} versus threshold shear Reynolds number R_{*c} and (*b*) threshold movability number M_{*c} versus particle Reynolds number $\mathscr{R}$, obtained from $M_{*c}(R_{*c})$ relationships. (Online version in colour.)

Paphitis [102] introduced the threshold movability number M_{*c}, defined as the ratio of the threshold shear velocity u_{*c} to the terminal fall velocity w_t, to study the effects of the terminal fall velocity w_t on the threshold bed shear stress τ_{bc} $(= \rho_f u_{*c}^2)$ in terms of the threshold shear Reynolds number R_{*c}. Figure 11*a* depicts the threshold movability number $M_{*c}(= u_{*c}/w_t)$ as a function of the threshold shear Reynolds number R_{*c} [102]. The lower bound, mean and upper bound curves, given by Paphitis [102], are expressed, respectively, as

$$\left.\begin{aligned} M_{*c}(0.1 < R_{*c} < 10^5) &= 0.078 + 0.01 \ln R_{*c} + 12 \exp(-2.5R_{*c}) + \frac{0.65}{R_{*c}}, \\ M_{*c}(0.1 < R_{*c} < 10^5) &= 0.115 + 0.01 \ln R_{*c} + 14 \exp(-2R_{*c}) + \frac{0.75}{R_{*c}} \\ \text{and} \quad M_{*c}(0.1 < R_{*c} < 10^5) &= 0.18 + 0.01 \ln R_{*c} + 14 \exp(-1.5R_{*c}) + \frac{0.88}{R_{*c}}. \end{aligned}\right\} \tag{6.3}$$

Importantly, figure 11*a* does not render a straightforward estimation of the threshold bed shear stress τ_{bc}, because the threshold shear velocity u_{*c} is involved in both the independent and dependent variables, R_{*c} and M_{*c}, respectively. To resolve this issue, the threshold movability number M_{*c} $(= u_{*c}/w_t)$ can be plotted as a function of particle Reynolds number $\mathscr{R}$ $(= R_{*c}/M_{*c})$, as shown in figure 11*b*. For a given particle size d, the terminal fall velocity w_t can be estimated using one of the empirical formulae. Once the particle Reynolds number $\mathscr{R}(= w_t d/\nu)$ is obtained, the threshold shear velocity u_{*c} and, in turn, the threshold bed shear stress $\tau_{bc}(= \rho_f u_{*c}^2)$ can be obtained from figure 11*b*.

Some researchers expressed the threshold movability number M_{*c} as a function of particle parameter D_* (figure 12). Using the experimental data, Beheshti & Ataie-Ashtiani [103] obtained the threshold movability number M_{*c} as

$$M_{*c}(D_* \leq 10) = 9.667 D_*^{-1.57} \quad \text{and} \quad M_{*c}(D_* > 10) = 0.474 D_*^{-0.226}. \tag{6.4}$$

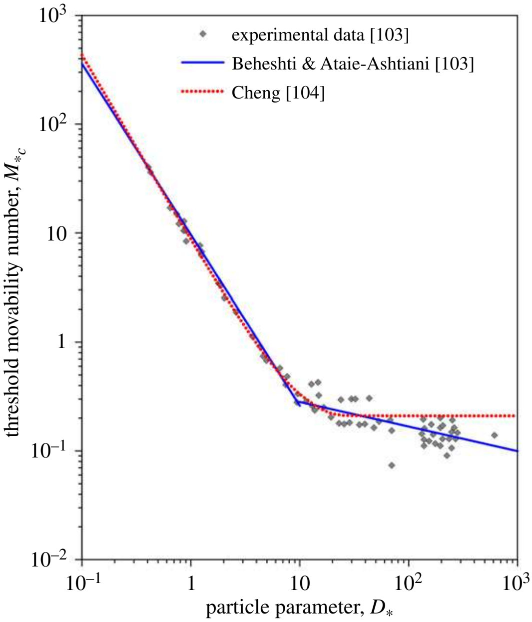

Figure 12. Threshold movability number M_{*c} versus particle parameter D_*. (Online version in colour.)

In addition, Cheng [104] applied an interpolation function in the form of a power sum and expressed the threshold movability number M_{*c} as (also see figure 12)

$$M_{*c} = 0.21\left[1 + \left(0.76 + \frac{41}{D_*^{1.7}}\right)^{20}\right]^{1/20}. \tag{6.5}$$

(b) Hydrodynamics of bedload transport

When the bed shear stress τ_b exceeds its threshold value τ_{bc}, the surface sediment particles are transported in various modes; for instance, rolling, sliding and lifting modes, collectively called the *bedload transport*. Einstein [105] was the pioneer to propose a semi-theoretical formulation of the bedload flux. In the mathematical analysis, Einstein [105] equated the number of entrained particles N_E with the number of deposited particles N_D per unit time and bed area. N_E and N_D can be expressed as

$$N_E = \frac{I_e}{k_2 d^2}\frac{P_E}{t_e} \tag{6.6a}$$

and

$$N_D = \frac{G_b I_d(1-P_E)}{l_x \rho_p g k_1 d^3} = \frac{G_b I_d(1-P_E)}{\lambda_x \rho_p g k_1 d^4}, \tag{6.6b}$$

where I_e is the bedload fraction to be entrained, k_2 is a factor related to the projected area of the particle, P_E is the entrainment probability in lifting mode, t_e is the exchange time, G_b is the bedload flux in dry weight (per unit time and bed width), I_d is the bedload fraction to be deposited, l_x is the mean saltation length ($=\lambda_x d$), λ_x is a constant (≈ 100 for spherical particles) and k_1 is a factor related to the particle volume.

Balancing equations (6.6*a*) and (6.6*b*), the bedload flux can be obtained as

$$G_b = \rho_p g d^2\left(\frac{P_E}{1-P_E}\right)\frac{I_e}{I_d}\frac{\lambda_x k_1}{k_2}\frac{1}{t_e}. \tag{6.7}$$

The entrainment probability P_E in lifting mode can be readily obtained by considering the fluid lift F_L surpassing the submerged weight F_G of the particle. It follows that $P_E = P_E(F_L \geq F_G)$.

However, the most important parameter in equation (6.7) is the exchange time t_e. In fact, Einstein [105] assumed the exchange time t_e to be proportional to the ratio of particle size d to terminal fall velocity w_t as

$$t_e \propto \frac{d}{w_t} \Longrightarrow t_e = k_3 \frac{d}{w_t}, \tag{6.8}$$

where k_3 is the proportionality constant. The fundamental rationale behind equation (6.8) is that, since the terminal fall velocity of a coarser particle is larger than that of a finer particle, specifically in the Stokesian realm (see equation (5.1)), the exchange time for the former is less than that for the latter. However, from the perspective of bedload transport, this observation is not physically feasible, because a coarser particle requires a longer time to reach its destination. To resolve this anomaly, Zee & Zee [106] modified equation (6.8) as

$$t_e \propto \frac{w_t}{g} \Longrightarrow t_e = k_3 \frac{w_t}{g}. \tag{6.9}$$

Both equations (6.8) and (6.9) highlight the subtle effects of terminal fall velocity w_t on the determination of bedload flux.

The prominent role of terminal fall velocity w_t on the bedload flux is also reflected from Bagnold's [107] mathematical analysis. Bagnold [107] considered a force balance between fluid drag and bed frictional resistance to express the bedload flux G_b as

$$G_b = \left(1 + \frac{1}{\Delta}\right)\left(1 - \frac{u_{*c}}{u_*}\right)\frac{\tau_0 U_f}{\tan \phi_d}\left[1 - \frac{1}{\kappa}\frac{u_*}{U_f}\ln\left(\frac{0.4h}{m_1 d}\right) - \frac{w_t}{U_f}\right], \tag{6.10}$$

where κ is the von Kármán coefficient ($= 0.41$) and m_1 is the ratio of mean saltation height to particle size.

(c) Hydrodynamics of suspended load transport

In a turbulent flow over a loose streambed, when the bed shear stress τ_b becomes much larger than the threshold bed shear stress τ_{bc}, turbulence in the near-bed flow zone is to lift up the finer sediment particles (figure 13). Eventually, the finer particles travel beyond the bedload layer and are maintained in suspension. Under such circumstances, the particles are bounded by the fluid parcel over an adequately long duration. Bagnold [108] found that the sediment particles remain in suspension when the shear velocity u_* surpasses 0.8 times the terminal fall velocity w_t ($M_* > 0.8$). The suspended particles transport upwards in a convective manner motivated by the vertical velocity fluctuations and, thereafter, they commingle with the neighbouring fluid. Importantly, the terminal fall velocity w_t of particles plays a delicate role in governing the dynamic equilibrium of sediment suspension, because the affinity of a particle to settle is balanced by the turbulent diffusion in the vertical direction. A comprehensive survey on the suspended load transport was reviewed elsewhere [6,109,110].

The impact of terminal fall velocity on the hydrodynamics of sediment suspension can be viewed from three different perspectives—determinations of the vertical distribution of a suspended sediment concentration, suspended load flux and the probability of a sediment particle remaining in suspension. These aspects are furnished below.

(i) Determination of the vertical distribution of a suspended sediment concentration

Under a steady-state condition, the sediment particles remain in suspension triggered by the vertical velocity fluctuations w' of a turbulent eddy, which has a velocity scale v_l (figure 13). On the other hand, owing to gravity, the particles tend to settle with their terminal fall velocity w_t. The fluid parcel that carries the suspended particles in its core travels a distance $2l$ from a lower level to a higher level (figure 13). Denoting the concentration distribution as $C(z)$, the upward and downward sediment fluxes F_u (in volume per unit time and area) through a section SS are

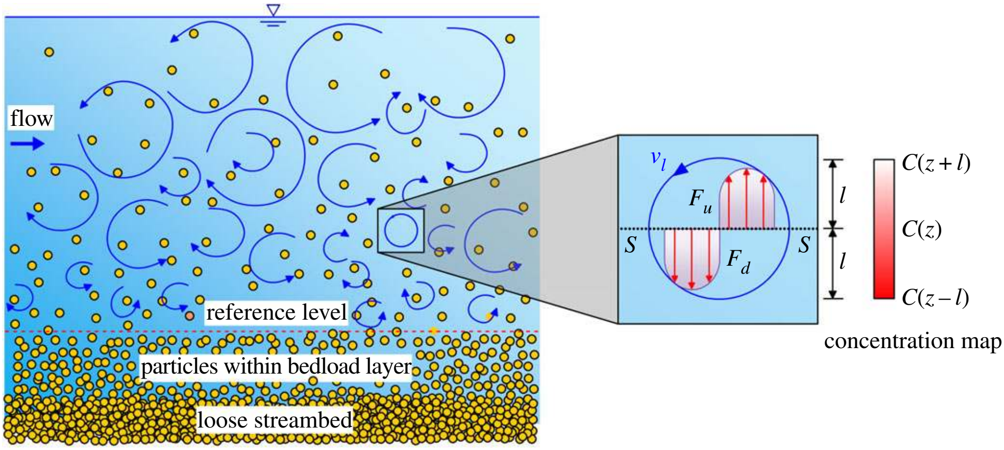

Figure 13. Schematic of the mechanism of sediment suspension in a turbulent flow. Curved arrows depict turbulent eddies carrying the suspended particles. (Online version in colour.)

expressed as

$$F_u = (w' - w_t)C(z - l) = (w' - w_t)\left(C - l\frac{\partial C}{\partial z}\right) \tag{6.11a}$$

and

$$F_d = (w' + w_t)C(z + l) = (w' + w_t)\left(C + l\frac{\partial C}{\partial z}\right). \tag{6.11b}$$

The dynamic equilibrium suggests $F_u = F_d$. It therefore produces

$$w'l\frac{\partial C}{\partial z} = -Cw_t. \tag{6.12}$$

In equation (6.12), the term $w'l$ is approximated as $w'l \approx \varepsilon_t/S_c$, where ε_t is the turbulent diffusivity and S_c is the *turbulent Schmidt number*. Therefore, equation (6.12) takes the form

$$\frac{\varepsilon_t}{S_c}\frac{\mathrm{d}C}{\mathrm{d}z} + Cw_t = 0. \tag{6.13}$$

The turbulent diffusivity ε_t is expressed as follows [6]:

$$\varepsilon_t = \kappa u_* z\left(1 - \frac{z}{h}\right). \tag{6.14}$$

Substituting equation (6.14) into equation (6.13) and integrating the resulting expression yields

$$C^+ = \left(\frac{1 - z^+}{z^+}\frac{z_r^+}{1 - z_r^+}\right)^{S_c/(\kappa M_*)}, \tag{6.15}$$

where C^+ is C/C_r, C_r is the reference concentration at a reference level $z = z_r$ (also see figure 13), z^+ is z/h and z_r^+ is z_r/h. Equation (6.15) provides the concentration distribution in the vertical direction. Equation (6.15) essentially reflects the role of terminal fall velocity w_t in governing the concentration distribution, because the movability number M_* explicitly takes into account the effects of the terminal fall velocity w_t.

In equation (6.15), it is a common practice to consider $S_c = 1$. To highlight the effects of the terminal fall velocity w_t on the concentration distribution, the non-dimensional concentration C^+ as a function of the non-dimensional vertical distance $(z^+ - z_r^+)/(1 - z_r^+)$, obtained from equation (6.15), is plotted in figure 14 for different values of movability number M_* (see solid lines for $M_* = 2, 4, 6, 8, 10, 20$ and 40). To prepare figure 14, we consider $z_r^+ = 0.05$. It appears that, for small values of movability number M_*, the concentration decreases abruptly as the vertical

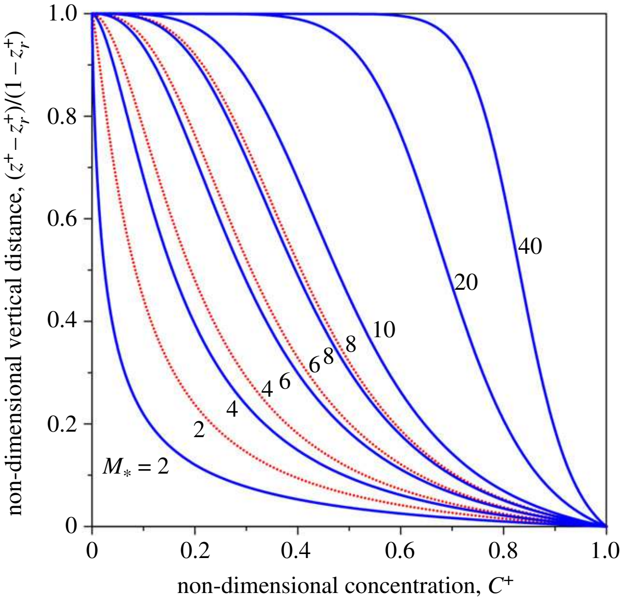

Figure 14. Non-dimensional vertical distance $(z^+ - z_r^+)/(1 - z_r^+)$ versus non-dimensional concentration C^+ for different values of movability number M_*. Solid lines correspond to the turbulent Schmidt number $S_c = 1$, while dotted lines correspond to the turbulent Schmidt numbers S_c obtained from equation (6.16). (Online version in colour.)

distance increases. Conversely, for large values of movability number M_*, the concentration reduces gradually with an increase in vertical distance. It is worth emphasizing that the distributional pattern of sediment concentration is principally controlled by the terminal fall velocity w_t and the shear velocity u_*. It turns out that, for a given shear velocity u_*, small and large values of movability number M_* correspond to coarser and finer sediment particles, respectively. On the other hand, for a given terminal fall velocity w_t (that is, for a given particle size d), a reduction in shear velocity u_* leads to a decrease in movability number M_*, resulting in a rapid diminution of sediment concentration with the vertical distance (figure 14).

Experimental results have evidenced that the turbulent Schmidt number S_c depends on the terminal fall velocity w_t. To be specific, van Rijn [111] expressed the Schmidt number S_c as a function of movability number M_* as

$$S_c(1 < M_* < 10) = \frac{M_*^2}{2 + M_*^2}. \tag{6.16}$$

Equation (6.16) can be readily substituted into equation (6.15) to obtain the non-dimensional concentration C^+ as a function of the non-dimensional vertical distance $(z^+ - z_r^+)/(1 - z_r^+)$. The resulting concentration distributions are plotted in figure 14 for different values of movability number M_* (see dotted lines for $M_* = 2,\ 4,\ 6$ and 8). Note that, as the above formula is limited to a specific range of movability number M_* $(1 < M_* < 10)$, only four values of M_* are shown in figure 14. It is apparent that the concentration distributions for S_c equalling unity and those obtained from equation (6.16) are alike for movability number $M_* = 8$. However, this difference is significant for a lower value of movability number M_*; for instance, $M_* = 2$.

In addition, Velikanov [112,113] pioneered the gravitational theory of sediment suspension, where fluid and solid phases were treated separately. The energy equation for the fluid phase essentially reflects the contribution from the terminal fall velocity w_t. It is expressed as

$$\Delta\rho_f g(1 - C)Cw_t = \rho_f g(1 - C)\bar{u}S_f + \bar{u}\frac{\mathrm{d}}{\mathrm{d}z}[(1 - C)\tau_t], \tag{6.17}$$

where $\bar{u}$ is the time-averaged longitudinal flow velocity, S_f is the energy slope and τ_t is the Reynolds shear stress. The term on the left-hand side of equation (6.17) signifies the required amount of energy to retain the particles in suspension. In non-dimensional form, the concentration distribution in the vertical direction was obtained as

$$C^+ = \exp(-\beta_v Z_v), \quad \beta_v = \frac{\Delta\kappa w_t}{(ghS_f^3)^{1/2}} \quad \text{and} \quad Z_v = \int_{z_r^+}^{z^+} \frac{dz^+}{(1-z^+)\ln[1+(hz^+)/\Delta_k]}, \tag{6.18}$$

where Δ_k is the roughness parameter. In the above, the terminal fall velocity w_t governs the parameter β_v and in turn the non-dimensional sediment concentration C^+.

(ii) Determination of the suspended load flux

The suspended load flux is estimated by integrating the product of the sediment concentration C and the time-averaged longitudinal flow velocity $\bar{u}$ over the flow depth h [6]. It can be expressed as the suspended load flux in volume per unit time and width Q_s or that in weight per unit time and width G_s. Q_s and G_s are expressed as

$$Q_s = \int_{z_r}^{h} C\bar{u}\,dz \quad \text{and} \quad G_s = \rho_p g \int_{z_r}^{h} C\bar{u}\,dz. \tag{6.19}$$

In order to obtain the depth-averaged concentration $\langle C\rangle$, Lane & Kalinske [114] integrated equation (6.15) over the entire flow depth. They expressed the suspended load flux Q_s as

$$Q_s = qC_rP_C \exp\left(\frac{15z_r^+}{M_*}\right), \tag{6.20}$$

where q is the fluid flux per unit channel width and P_C is the relative concentration ($=\langle C\rangle/C_r$). In the above, P_C was found to be dependent on the terminal fall velocity w_t. Lane & Kalinske [114] expressed the relative concentration P_C as a function of movability number M_* and $n_M/h^{1/6}$ (h is in inches), where n_M is the Manning roughness coefficient in SI units.

Figure 15*a* illustrates the relative concentration P_C as a function of movability number M_* for different values of $n_M/h^{1/6}$ ($=0.1,\ 0.2$ and 0.3), given by Lane & Kalinske [114]. It appears that, for a given movability number M_*, the relative concentration P_C decreases with an increase in $n_M/h^{1/6}$. In addition, for a given $n_M/h^{1/6}$, the relative concentration P_C increases as the movability number M_* increases. To shed light on the influence of the terminal fall velocity w_t on the suspended load flux Q_s, the relative suspended load flux $Q_s/(qC_r)$ as a function of movability number M_* for $n_M/h^{1/6} = 0.2$, obtained from equation (6.20) and figure 15*a*, is shown in figure 15*b*. Essentially, the relative suspended load flux $Q_s/(qC_r)$ increases with an increase in movability number M_*, because, for a given shear velocity u_*, the suspended sediment flux for finer particles is larger than that for coarser particles.

On the other hand, Bagnold [108] expressed the flow energetics to keep the particles in suspension as a product of the total submerged weight W_G of sediment particles and the terminal fall velocity w_t. Thus, the energy required to retain particles in suspension was expressed as

$$W_G w_t = \tau_b U_f (1-e_b) e_s, \tag{6.21}$$

where e_b and e_s are the efficiencies of bedload and suspended load transport. Using the experimental data, Bagnold [108] finally expressed the suspended load flux G_s as a function of the terminal fall velocity w_t as

$$G_s = 0.01\tau_b \left(1+\frac{1}{\Delta}\right)\frac{U_f^2}{w_t}. \tag{6.22}$$

(iii) Determination of the probability of a sediment particle remaining in suspension

The terminal fall velocity w_t can be used to determine the probability of a sediment particle remaining in suspension. Here, the central idea is to find the probability P_S of vertical velocity

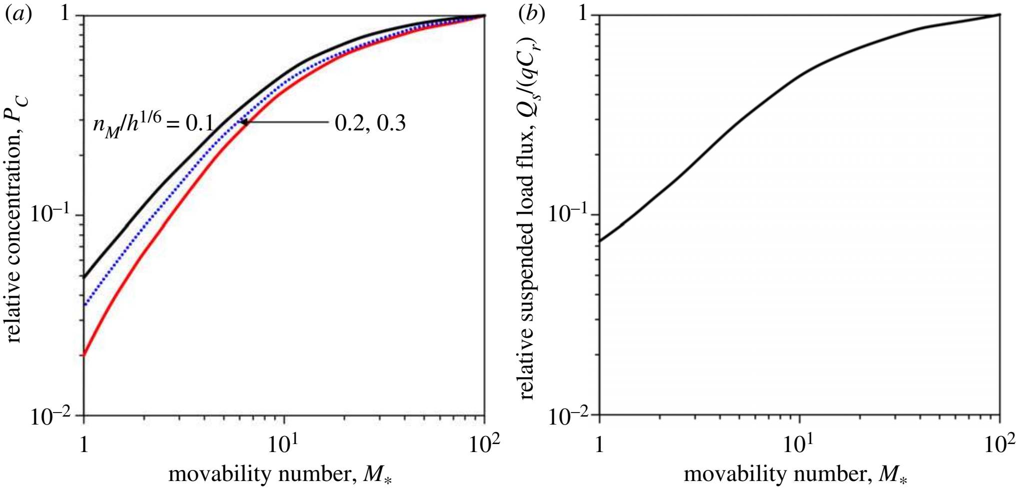

Figure 15. (*a*) Relative concentration P_C versus movability number M_* for different values of $n_M/h^{1/6}$ and (*b*) relative suspended load flux $Q_s/(qC_r)$ versus movability number M_* for $n_M/h^{1/6} = 0.2$. (Online version in colour.)

fluctuations w' surpassing the terminal fall velocity w_t. Cheng & Chiew [115] assumed the vertical velocity fluctuations w' to follow a normal distribution. They obtained the probability P_S as

$$P_S = \frac{1}{2} - \frac{1}{2}\left[1 - \exp\left(-\frac{2}{\pi}\frac{w_t^2}{\overline{w'^2}}\right)\right]^{1/2}. \tag{6.23}$$

In the above, an over-bar denotes the time averaging. On the other hand, considering the vertical velocity fluctuations w' to follow the Gram–Charlier series grounded on the Laplace distribution, Bose & Dey [116] expressed the probability P_S involving the terminal fall velocity w_t as

$$P_S = \frac{1}{16}\left(16 - \frac{w_t}{\sqrt{\overline{w'^2}}} - \frac{w_t^2}{\overline{w'^2}}\right)\exp\left(-\frac{w_t}{\sqrt{\overline{w'^2}}}\right). \tag{6.24}$$

7. Closure

In commemoration of Sir George Gabriel Stokes' two-hundredth birthday, this article has reviewed the essential elements of the terminal fall velocity from the standpoint of fluvial hydraulics, underlining the wealthy heritage that Stokes has left over the decades. From the perspective of both theoretical and empirical foundations, a comprehensive overview of the fluid drag on a particle in Stokesian, transitional and Newtonian realms has been elaborated. In addition, the generic force system governing the motion of a falling particle through a fluid and the subtle factors that control the terminal fall velocity have been critically appraised. From the perspective of fluvial hydraulics, the inextricable link of the terminal fall velocity with the hydrodynamics of sediment threshold, bedload transport and suspended load transport has been illuminated. The article has essentially brought into focus how an accurate estimation of the terminal fall velocity would lead to the application of the so-called empirical formulae with confidence in predicting the key aspects of the sediment transport phenomenon.

Among the key processes of sediment transport, the effects of the terminal fall velocity are reflected mostly on the hydrodynamics of sediment suspension. Despite magnificent advances in understanding the role of the terminal fall velocity in driving the mechanism of suspended particles, several key questions still require precise answers. Some of these questions include the following. How can the hindered settling exponent be determined from a theoretical background?

What could be the possible estimation of the terminal fall velocity for a strong sediment suspension? Which of nonlinear drag or the loitering effect is more significant in reducing the terminal fall velocity of a coarser particle? How does the terminal fall velocity influence the turbulent Schmidt number over a wide range of particle sizes? What is the precise response of the terminal fall velocity to various degrees of turbulence, such as weak, moderately strong and strong turbulence? These open questions not only show the subject's future research directions but also offer an insightful glance into the most fundamental research aspects. To resolve the above-mentioned issues, researchers need to rethink how the most fundamental description of fluid drag on a particle can be extended and applied to solve real-world problems. In this regard, analytical, experimental and numerical frameworks must work together to find the most satisfactory answers to the current challenges.

Data accessibility. This paper does not have any additional data.
Authors' contributions. The authors of this paper contributed jointly.
Competing interests. We declare we have no competing interests.
Funding. No funding has been received for this article.
Acknowledgements. S.D. acknowledges the JC Bose Fellowship Award in pursuing this work.

References

1. Stokes GG. 1851 On the effect of the internal friction of fluids on the motion of pendulums. *Trans. Camb. Phil. Soc.* **9**, 8–106.
2. Dusenbery DB. 2009 *Living at micro scale: the unexpected physics of being small*. Cambridge, MA: Harvard University Press.
3. Costa A, Folch A, Macedonio G. 2010 A model for wet aggregation of ash particles in volcanic plumes and clouds: 1. Theoretical formulation. *J. Geophys. Res. Solid Earth* **115**, B09201.
4. Carazzo G, Jellinek AM. 2013 Particle sedimentation and diffusive convection in volcanic ash-clouds. *J. Geophys. Res. Solid Earth* **118**, 1420–1437. (doi:10.1002/jgrb.50155)
5. Farrell EJ, Sherman DJ. 2015 A new relationship between grain size and fall (settling) velocity in air. *Prog. Phys. Geogr.* **39**, 361–387. (doi:10.1177/0309133314562442)
6. Dey S. 2014 *Fluvial hydrodynamics: hydrodynamic and sediment transport phenomena*. Berlin, Germany: Springer.
7. Rayleigh L. 1905 Obituary notice. In *George Gabriel Stokes, Mathematical and Physical Papers*. Cambridge, UK: Cambridge University Press.
8. Schultz EF, Wilde RH, Albertson ML. 1954 Influence of shape on the fall velocity of sedimentary particles. Missouri River Division, Corps of Engineers, US Army, Omaha, NE.
9. Briggs LI, McCulloch DS, Moser F. 1962 The hydraulic shape of sand particles. *J. Sediment. Res.* **32**, 645–656.
10. Engelund F, Hansen E. 1967 A monograph on sediment transport in alluvial streams. Technical University of Denmark, Copenhagen, Denmark.
11. Komar PD, Reimers CE. 1978 Grain shape effects on settling rates. *J. Geol.* **86**, 193–209. (doi:10.1086/649674)
12. Hallermeier RJ. 1981 Terminal settling velocity of commonly occurring sand grains. *Sedimentology* **28**, 859–865. (doi:10.1111/j.1365-3091.1981.tb01948.x)
13. Cheng N-S. 1997 Simplified settling velocity formula for sediment particle. *J. Hydraul. Eng.* **123**, 149–152. (doi:10.1061/(ASCE)0733-9429(1997)123:2(149))
14. Raudkivi AJ. 1998 *Loose boundary hydraulics*. Rotterdam, The Netherlands: Balkema.
15. Paphitis D, Collins MB, Nash LA, Wallbridge S. 2002 Settling velocities and entrainment thresholds of biogenic sands (shell fragments) under unidirectional flow. *Sedimentology* **49**, 211–225. (doi:10.1046/j.1365-3091.2002.00446.x)
16. She K, Trim L, Pope D. 2005 Fall velocities of natural sediment particles: a simple mathematical presentation of the fall velocity law. *J. Hydraul. Res.* **43**, 189–195. (doi:10.1080/00221686.2005.9641235)
17. Rieux A, Weill P, Mouaze D, Poirier C, Nechenache F, Perez L, Tessier B. 2019 Threshold of motion and settling velocities of mollusc shell debris: influence of faunal composition. *Sedimentology* **66**, 895–916. (doi:10.1111/sed.12521)
18. Whitehead N. 1889 Second approximations to viscous fluid motion. *Quart. J. Math.* **23**, 143–152.

19. Oseen CW. 1910 Über die Stokes'sche formel und über eine verwandte aufgabe in der hydrodynamik. *Arkiv för Matematik, Astronomi och Fysik* **6**, paper 29, 1–20.
20. Oseen CW. 1913 Über den gültigkeitsbereich der Stokesschen widerstandsformel. *Arkiv för Matematik, Astronomi och Fysik* **9**, paper 16, 1–15.
21. Goldstein S. 1929 The steady flow of viscous fluid past a fixed spherical obstacle at small Reynolds numbers. *Proc. R. Soc. Lond. A* **123**, 225–235. (doi:10.1098/rspa.1929.0067)
22. Goldstein S. 1938 *Modern developments in fluid dynamics*, vol. 2. New York, NY: Dover Publications.
23. Tomotika S, Aoi T. 1950 The steady flow of viscous fluid past a sphere and circular cylinder at small Reynolds numbers. *Q. J. Mech. Appl. Math.* **3**, 140–161. (doi:10.1093/qjmam/3.2.141)
24. Stewartson K. 1956 On the steady flow past a sphere at high Reynolds number using Oseen's approximation. *Phil. Mag.* **1**, 345–354. (doi:10.1080/14786435608238108)
25. Proudman I, Pearson JRA. 1957 Expansions at small Reynolds numbers for the flow past a sphere and a circular cylinder. *J. Fluid Mech.* **2**, 237–262. (doi:10.1017/S0022112057000105)
26. Chester W, Breach DR, Proudman I. 1969 On the flow past a sphere at low Reynolds number. *J. Fluid Mech.* **37**, 751–760. (doi:10.1017/S0022112069000851)
27. Abraham FF. 1970 Functional dependence of drag coefficient of a sphere on Reynolds number. *Phys. Fluids* **13**, 2194–2195. (doi:10.1063/1.1693218)
28. van Dyke M. 1970 Extension of Goldstein's series for the Oseen drag of a sphere. *J. Fluid Mech.* **44**, 365–372. (doi:10.1017/S0022112070001878)
29. Hunter C, Lee SM. 1986 The analytic structure of Oseen flow past a sphere as a function of Reynolds number. *SIAM J. Appl. Math.* **46**, 978–999. (doi:10.1137/0146058)
30. Weisenborn AJ, Bosch BIMT. 1993 Analytical approach to the Oseen drag on a sphere at infinite Reynolds number. *SIAM J. Appl. Math.* **53**, 601–620. (doi:10.1137/0153031)
31. Liao S-J. 2002 An analytic approximation of the drag coefficient for the viscous flow past a sphere. *Int. J. Non-Linear Mech.* **37**, 1–18. (doi:10.1016/S0020-7462(00)00092-5)
32. Mikhailov MD, Silva Freire AP. 2013 The drag coefficient of a sphere: an approximation using Shanks transform. *Powder Technol.* **237**, 432–435. (doi:10.1016/j.powtec.2012.12.033)
33. Rubey W. 1933 Settling velocities of gravel, sand and silt particles. *Am. J. Sci.* **5**, 325–338. (doi:10.2475/ajs.s5-25.148.325)
34. Guo J. 2011 Motion of spheres falling through fluids. *J. Hydraul. Res.* **49**, 32–41. (doi:10.1080/00221686.2010.538572)
35. Schiller L, Naumann A. 1933 Über die grundlegen berechnungen bei der schwerkraftaufbereitung. *Zeitschrift des Vereines Deutscher Ingenieure* **77**, 318–320.
36. Dou GR. 1981 *Turbulence mechanics*. Beijing, China: People's Education Press.
37. Concha F, Barrientos A. 1982 Settling velocities of particulate systems, 3. Power-series expansion for the drag coefficient of a sphere and prediction of the settling velocity. *Int. J. Miner. Process.* **9**, 167–172. (doi:10.1016/0301-7516(82)90025-4)
38. Flemmer RLC, Banks CL. 1986 On the drag coefficient of a sphere. *Powder Technol.* **48**, 217–221. (doi:10.1016/0032-5910(86)80044-4)
39. Turton R, Levenspiel OA. 1986 Short note on the drag correlation for spheres. *Powder Technol.* **47**, 83–86. (doi:10.1016/0032-5910(86)80012-2)
40. Fredsøe J, Deigaard R. 1992 *Mechanics of coastal sediment transport*. Singapore: World Scientific.
41. Ceylan K, Altunbaş A, Kelbaliyev G. 2001 A new model for estimation of drag force in the flow of Newtonian fluids around rigid or deformable particles. *Powder Technol.* **119**, 250–256. (doi:10.1016/S0032-5910(01)00261-3)
42. Brown PP, Lawler DF. 2003 Sphere drag and settling velocity revisited. *J. Environ. Eng.* **129**, 222–231. (doi:10.1061/(ASCE)0733-9372(2003)129:3(222))
43. Fidleris V, Whitmore RL. 1961 Experimental determination of the wall effect for spheres falling axially in cylindrical vessels. *Br. J. Appl. Phys.* **12**, 490–494. (doi:10.1088/0508-3443/12/9/311)
44. Almedeij J. 2008 Drag coefficient of flow around a sphere: matching asymptotically the wide trend. *Powder Technol.* **186**, 218–223. (doi:10.1016/j.powtec.2007.12.006)
45. Cheng N-S. 2009 Comparison of formulas for drag coefficient and settling velocity of spherical particles. *Powder Technol.* **189**, 395–398. (doi:10.1016/j.powtec.2008.07.006)
46. Yang H, Fan M, Liu A, Dong L. 2015 General formulas for drag coefficient and settling velocity of sphere based on theoretical law. *Int. J. Min. Sci. Technol.* **25**, 219–223. (doi:10.1016/j.ijmst.2015.02.009)

47. Rouse H. 1938 *Fluid mechanics for hydraulic engineers*. New York, NY: Dover Publishers.
48. Yaghoobi H, Torabi M. 2012 Novel solution for acceleration motion of a vertically falling non-spherical particle by VIM–Padé approximant. *Powder Technol.* **215–216**, 206–209. (doi:10.1016/j.powtec.2011.09.049)
49. Yaghoobi H, Torabi M. 2012 Analytical solution for settling of non-spherical particles in incompressible Newtonian media. *Powder Technol.* **221**, 453–463. (doi:10.1016/j.powtec.2012.01.044)
50. Dogonchi AS, Hatami M, Hosseinzadeh Kh, Domairry G. 2015 Non-spherical particles sedimentation in an incompressible Newtonian medium by Padé approximation. *Powder Technol.* **278**, 248–256. (doi:10.1016/j.powtec.2015.03.036)
51. Dietrich WE. 1982 Settling velocity of natural particles. *Water Resour. Res.* **18**, 1615–1626. (doi:10.1029/WR018i006p01615)
52. Ahrens JP. 2000 A fall-velocity equation. *J. Waterw. Port Coastal Ocean Eng.* **126**, 99–102. (doi:10.1061/(ASCE)0733-950X(2000)126:2(99))
53. Jiménez JA, Madsen OS. 2003 A simple formula to estimate settling velocity of natural sediments. *J. Waterw. Port Coastal Ocean Eng.* **129**, 70–78. (doi:10.1061/(ASCE)0733-950X(2003)129:2(70))
54. Mrokowska MM. 2018 Stratification-induced reorientation of disk settling through ambient density transition. *Sci. Rep.* **8**, 412. (doi:10.1038/s41598-017-18654-7)
55. Fornari W, Ardekani MN, Brandt L. 2018 Clustering and increased settling speed of oblate particles at finite Reynolds number. *J. Fluid Mech.* **848**, 696–721. (doi:10.1017/jfm.2018.370)
56. Jucha J, Naso A, Lévêque E, Pumir A. 2018 Settling and collision between small ice crystals in turbulent flows. *Phys. Rev. Fluids* **3**, 014604. (doi:10.1103/PhysRevFluids.3.014604)
57. Langleben MP. 1954 The terminal velocity of snowflakes. *Q. J. R. Meteor. Soc.* **80**, 174–181. (doi:10.1002/qj.49708034404)
58. Lee J-E, Jung S-H, Park H-M, Kwon S, Lin P-L, Lee GW. 2015 Classification of precipitation types using fall velocity–diameter relationships from 2D-video distrometer measurements. *Adv. Atmos. Sci.* **32**, 1277–1290. (doi:10.1007/s00376-015-4234-4)
59. Li J, Osada K. 2007 Preferential settling of elongated mineral dust particles in the atmosphere. *Geophys. Res. Lett.* **34**, L17807. (doi:10.1029/2007GL030262)
60. Del Bello E, Taddeucci J, de' Michieli Vitturi M, Scarlato P, Andronico D, Scollo S, Kueppers U, Ricci T. 2017 Effect of particle volume fraction on the settling velocity of volcanic ash particles: insights from joint experimental and numerical simulations. *Sci. Rep.* **6**, 39620. (doi:10.1038/srep39620)
61. Clift R, Grace JR, Weber ME. 1978 *Bubbles, drops and particles*. New York, NY: Academic Press.
62. Başağaoğlu H, Succi S, Wyrick D, Blount J. 2018 Particle shape influences settling and sorting behavior in microfluidic domains. *Sci. Rep.* **8**, 8583. (doi:10.1038/s41598-018-26786-7)
63. Middleton GV, Southard JB. 1978 Mechanics of sediment movement. Lecture notes for Short Course, no. 3, pp. 248. Eastern Section of the Soc. of Econ. Paleontol. and Mineralog., Binghampton, NY.
64. Gustavsson K, Jucha J, Naso A, Lévêque E, Pumir A, Mehlig B. 2017 Statistical model for the orientation of nonspherical particles settling in turbulence. *Phys. Rev. Lett.* **119**, 254501. (doi:10.1103/PhysRevLett.119.254501)
65. Wu W, Wang SSY. 2006 Formulas for sediment porosity and settling velocity. *J. Hydraul. Eng.* **132**, 858–862. (doi:10.1061/(ASCE)0733-9429(2006)132:8(858))
66. Camenen B. 2007 Simple and general formula for the settling velocity of particles. *J. Hydraul. Eng.* **133**, 229–233. (doi:10.1061/(ASCE)0733-9429(2007)133:2(229))
67. Richardson JF, Zaki WN. 1954 Sedimentation and fluidisation, part I. *Trans. Inst. Chem. Eng.* **32**, 35–53.
68. Wilhelm RH, Kwauk M. 1948 Fluidization of solid particles. *Chem. Eng. Prog.* **44**, 201–218.
69. Jottrand R. 1952 An experimental study of the mechanism of fluidisation. *J. Appl. Chem.* **2**, S17–S26.
70. Cleasby JL, Woods CF. 1975 Intermixing of dual media and multi-media granular filters. *J. Am. Water Works Assoc.* **67**, 197–203. (doi:10.1002/j.1551-8833.1975.tb02195.x)
71. Baldock TE, Tomkins MR, Nielsen P, Hughes MG. 2004 Settling velocity of sediments at high concentrations. *Coast. Eng.* **51**, 91–100. (doi:10.1016/j.coastaleng.2003.12.004)
72. Yin X, Koch DL. 2007 Hindered settling velocity and microstructure in suspensions of solid spheres with moderate Reynolds numbers. *Phys. Fluids* **19**, 093302. (doi:10.1063/1.2764109)

73. Garside J, Al-Dibouni MR. 1977 Velocity-voidage relationships for fluidization and sedimentation in solid-liquid systems. *Ind. Eng. Chem. Process Des. Develop.* **16**, 206–214. (doi:10.1021/i260062a008)
74. Fouda AE, Capes CE. 1977 Hydrodynamic particle volume and fluidized bed expansion. *Can. J. Chem. Eng.* **55**, 386–391. (doi:10.1002/cjce.5450550404)
75. Cleasby JL, Fan K. 1981 Predicting fluidization and expansion of filter media. *J. Environ. Eng.* **107**, 455–471.
76. Tomkins MR, Baldock TE, Nielsen P. 2005 Hindered settling of sand grains. *Sedimentology* **52**, 1425–1432. (doi:10.1111/j.1365-3091.2005.00750.x)
77. Cheng N-S. 1997 Effect of concentration on settling velocity of sediment particles. *J. Hydraul. Eng.* **123**, 728–731. (doi:10.1061/(ASCE)0733-9429(1997)123:8(728))
78. Oliver DR. 1961 The sedimentation of suspensions of closely-sized spherical particles. *Chem. Eng. Sci.* **15**, 230–242. (doi:10.1016/0009-2509(61)85026-4)
79. Sha YQ. 1965 *Introduction to sediment dynamics*. Beijing, China: Industry Press.
80. Soulsby RL. 1997 *Dynamics of marine sands*. London, UK: Thomas Telford.
81. Wang L-P, Maxey MR. 1993 Settling velocity and concentration distribution of heavy particles in homogeneous isotropic turbulence. *J. Fluid Mech.* **256**, 27–68. (doi:10.1017/S0022112093002708)
82. Yang TS, Shy SS. 2003 The settling velocity of heavy particles in an aqueous near-isotropic turbulence. *Phys. Fluids* **15**, 868–880. (doi:10.1063/1.1557526)
83. Bec J, Homann H, Ray SS. 2014 Gravity-driven enhancement of heavy particle clustering in turbulent flow. *Phys. Rev. Lett.* **112**, 184501. (doi:10.1103/PhysRevLett.112.184501)
84. Good GH, Ireland PJ, Bewley GP, Bodenschatz E, Collins LR, Warhaft Z. 2014 Settling regimes of inertial particles in isotropic turbulence. *J. Fluid Mech.* **759**, R3. (doi:10.1017/jfm.2014.602)
85. Elhimer M, Praud O, Marchal M, Cazin S, Bazile R. 2017 Simultaneous PIV/PTV velocimetry technique in a turbulent particle-laden flow. *J. Vis.* **20**, 289–304. (doi:10.1007/s12650-016-0397-z)
86. van Hinsberg MAT, Clercx HJH, Toschi F. 2017 Enhanced settling of nonheavy inertial particles in homogeneous isotropic turbulence: the role of the pressure gradient and the Basset history force. *Phys. Rev. E* **95**, 023106. (doi:10.1103/PhysRevE.95.023106)
87. Huck PD, Bateson C, Volk R, Cartellier A, Bourgoin M, Aliseda A. 2018 The role of collective effects on settling velocity enhancement for inertial particles in turbulence. *J. Fluid Mech.* **846**, 1059–1075. (doi:10.1017/jfm.2018.272)
88. Petersen AJ, Baker L, Coletti F. 2019 Experimental study of inertial particles clustering and settling in homogeneous turbulence. *J. Fluid Mech.* **864**, 925–970. (doi:10.1017/jfm.2019.31)
89. Tom J, Bragg AD. 2019 Multiscale preferential sweeping of particles settling in turbulence. *J. Fluid Mech.* **871**, 244–270. (doi:10.1017/jfm.2019.337)
90. Nielsen P. 1993 Turbulence effects on the settling of suspended particles. *J. Sediment. Petrol.* **63**, 835–838.
91. Kawanisi K, Shiozaki R. 2008 Turbulent effects on the settling velocity of suspended sediment. *J. Hydraul. Eng.* **134**, 261–266. (doi:10.1061/(ASCE)0733-9429(2008)134:2(261))
92. Fornari W, Picano F, Sardina G, Brandt L. 2016 Reduced particle settling speed in turbulence. *J. Fluid Mech.* **808**, 153–167. (doi:10.1017/jfm.2016.648)
93. Momenifar M, Dhariwal R, Bragg AD. 2019 Influence of Reynolds number on the motion of settling, bidisperse inertial particles in turbulence. *Phys. Rev. Fluids* **4**, 054301. (doi:10.1103/PhysRevFluids.4.054301)
94. Chouippe A, Uhlmann M. 2019 On the influence of forced homogeneous-isotropic turbulence on the settling and clustering of finite-size particles. *Acta Mech.* **230**, 387–412. (doi:10.1007/s00707-018-2271-7)
95. Fornari W, Zade S, Brandt L, Picano F. 2019 Settling of finite-size particles in turbulence at different volume fractions. *Acta Mech.* **230**, 413–430. (doi:10.1007/s00707-018-2269-1)
96. Wang Y, Lam KM, Lu Y. 2018 Settling velocity of fine heavy particles in turbulent open channel flow. *Phys. Fluids* **30**, 095106. (doi:10.1063/1.5046333)
97. Nielsen P. 1984 On the motion of suspended particles. *J. Geophys. Res. Oceans* **89**, 616–626. (doi:10.1029/JC089iC01p00616)
98. Tooby PF, Wick GL, Isaacs JD. 1977 The motion of a small sphere in a rotating velocity field: a possible mechanism for suspending particles in turbulence. *J. Geophys. Res. Oceans Atmos.* **82**, 2096–2100. (doi:10.1029/JC082i015p02096)

99. Maxey MR, Corrsin S. 1986 Gravitational settling of aerosol particles in randomly oriented cellular flow fields. *J. Atmos. Sci.* **43**, 1112–1134. (doi:10.1175/1520-0469(1986)043<1112:GSOAPI>2.0.CO;2)
100. Dey S, Ali SZ. 2019 Bed sediment entrainment by streamflow: state of the science. *Sedimentology* **66**, 1449–1485. (doi:10.1111/sed.12566)
101. Yang CT. 1973 Incipient motion and sediment transport. *J. Hydraul. Div.* **99**, 1679–1704.
102. Paphitis D. 2001 Sediment movement under unidirectional flows: an assessment of empirical threshold curves. *Coast. Eng.* **43**, 227–245. (doi:10.1016/S0378-3839(01)00015-1)
103. Beheshti AA, Ataie-Ashtiani B. 2008 Analysis of threshold and incipient conditions for sediment movement. *Coast. Eng.* **55**, 423–430. (doi:10.1016/j.coastaleng.2008.01.003)
104. Cheng N-S. 2008 Comparison of settling-velocity-based formulas for threshold of sediment motion. *J. Hydraul. Eng.* **134**, 1136–1141. (doi:10.1061/(ASCE)0733-9429(2008)134:8(1136))
105. Einstein HA. 1950 The bed-load function for sediment transportation in open channel flows. Technical bulletin 1026, United States Department of Agriculture, Soil Conservation Service, Washington, DC.
106. Zee C-H, Zee R. 2017 Formulas for the transportation of bed load. *J. Hydraul. Eng.* **143**, 04016101. (doi:10.1061/(ASCE)HY.1943-7900.0001248)
107. Bagnold RA. 1956 The flow of cohesionless grains in fluids. *Phil. Trans. R. Soc. Lond. A* **249**, 235–297. (doi:10.1098/rsta.1956.0020)
108. Bagnold RA. 1966 An approach to the sediment transport problem from general physics. Geological survey professional paper 422-I, Washington, DC. See https://pubs.usgs.gov/pp/0422i/report.pdf.
109. Ali SZ, Dey S. 2016 Mechanics of advection of suspended particles in turbulent flow. *Proc. R. Soc. A* **472**, 20160749. (doi:10.1098/rspa.2016.0749)
110. Dey S, Ali SZ, Padhi E. 2018 Advances in analytical modeling of suspended sediment transport. *J. Hydro-environ. Res.* **20**, 110–126. (doi:10.1016/j.jher.2018.02.004)
111. van Rijn LC. 1984 Sediment transport, part II: suspended load transport. *J. Hydraul. Eng.* **110**, 1613–1641. (doi:10.1061/(ASCE)0733-9429(1984)110:11(1613))
112. Velikanov MA. 1954 Principle of the gravitational theory of the movement of sediments. *Acad. Sci. Bull. Geophys. Ser.* **4**, 349–359.
113. Velikanov MA. 1958 *Alluvial process (fundamental principles)*. Moscow, Russia: State Publishing House of Theoretical and Technical Literature.
114. Lane EW, Kalinske AA. 1941 Engineering calculations of suspended sediment. *Trans. Am. Geophys. Union* **20**, 603–607. (doi:10.1029/TR022i003p00603)
115. Cheng N-S, Chiew Y-M. 1999 Analysis of initiation of sediment suspension from bed load. *J. Hydraul. Eng.* **125**, 855–861. (doi:10.1061/(ASCE)0733-9429(1999)125:8(855))
116. Bose SK, Dey S. 2013 Sediment entrainment probability and threshold of sediment suspension: exponential-based approach. *J. Hydraul. Eng.* **139**, 1099–1106. (doi:10.1061/(ASCE)HY.1943-7900.0000763)